CMS Analysis Note

The content of this note is intended for CMS internal use and distribution only

1 December 2006

Search for decaying in flight neutralinos and long lived staus within Gauge Mediated Supersymmetry Breaking models

Łukasz Gościło, Piotr Traczyk, Piotr Zalewski

Soltan Institute for Nuclear Studies, Warsaw, Poland

Małgorzata Kazana

Laboratório de Instrumentação e Física Experimental de Partículas, Lisboa, Portugal

Abstract

Within Gauge-Mediated Supersymmetry Breaking (GMSB) models the gravitino is the Lightest Supersymmetry Partner (LSP) whereas the neutralino or stau play the role of the Next to Lightest Supersymmetry Partner (NLSP). NLSP decays to its Standard Model partner and a gravitino, with a lifetime depending on the scale of SUSY breaking. Detection of the NLSP and determination of its properties, lifetime in particular, can be of crucial importance for the physics program at the LHC. We concentrate on two scenarios giving nonstandard detector signatures. In the first one, a decaying in flight neutralino is the NLSP. We use photons not pointing to the interaction point, identified by the CMS electromagnetic calorimeter, as a signature of decaying in flight neutralinos. We show that it is possible to estimate the ctau of neutralinos in a range from centimeters to meters with a precision of the order of 20%, if the number of produced signal events is not less than about 5000. In the second case a long-lived stau is the NLSP. We show that the CMS muon system is able to detect it as a particle traveling with a velocity lower than the speed of light, and determine its mass. For both cases we estimate the minimal amount of integrated luminosity needed for a discovery in points chosen for detailed simulation.

1 Introduction

The idea of low-energy supersymmetry breaking is almost a quarter of a century old [1]. Here we present a very short introduction following reference [2].

In order to preserve supersymmetry in a theory which includes gravity, supersymmetry must be promoted to a local symmetry. For any local symmetry realized in the broken phase, the gauge particle becomes massive by eating the Nambu-Goldstone particle. With a spontaneously broken local supersymmetry, the spin $\frac{1}{2}$ Goldstino becomes the longitudinal components of the spin $\frac{3}{2}$ gravitino, the superpartner of the graviton. This super-Higgs mechanism gives a mass to the gravitino-Goldstino, given by

$$m_{\widetilde{G}} = \frac{F}{\sqrt{3}M_P} \simeq 2.4 \left(\frac{\sqrt{F}}{100 \text{ TeV}}\right)^2 \text{ eV}, \tag{1}$$

where $M_P = 2.4 \times 10^{18}$ GeV is the reduced Planck mass, and F is the order parameter for spontaneous supersymmetry breaking with units of [mass]^2. F is a vacuum expectation value (of an auxiliary field) which measures the magnitude of supersymmetry breaking in the vacuum state.

If the scale of supersymmetry breaking is not too high, these interactions can be relevant to accelerator physics. In particular a massive superpartner, $\widetilde{X}$, can decay to its partner particle, X, by emitting an essentially massless Goldstino with a decay rate of

$$\Gamma(\widetilde{X} \to X\widetilde{G}) = \frac{\kappa m_{\widetilde{X}}^5}{16\pi F^2} \left(1 - \frac{m_X^2}{m_{\widetilde{X}}^2}\right)^4, \tag{2}$$

where κ is a mixing parameter to be evaluated for a given set of model parameters. If X and $\widetilde{X}$ are unmixed states within the same supermultiplet, such as for slepton decay to a lepton and Goldstino, $\kappa = 1$. However, for superpartner mass eigenstates which are mixtures of superpartners in different supermultiplets, $\kappa < 1$ is possible. For a pure $U(1)_Y$ Bino decay to a photon and Goldstino, $\kappa = \cos^2 \theta_W$.

The above decay rate corresponds to a decay length of

$$c\tau(\widetilde{X} \to X\widetilde{G}) \simeq \left(\frac{1 \text{ m}}{\kappa}\right) \left(\frac{100 \text{ GeV}}{m_{\tilde{X}}}\right)^5 \left(\frac{\sqrt{F}}{1000 \text{ TeV}}\right)^4 \left(1 - \frac{m_X^2}{m_{\widetilde{X}}^2}\right)^{-4} \tag{3}$$

For a supersymmetry breaking scale, $\sqrt{F}$, much larger than a few 1000 TeV, superpartner decays through the Goldstino take place well outside the particle detector. A SUSY breaking scale which allows the decay to the Goldstino is generally referred to as low-scale supersymmetry breaking. The probability that an NLSP with a decay width Γ_{NLSP}, mass m_{NLSP}, and energy E in the lab frame will not decay before traveling a distance x is $P(x) = e^{-x/\beta\gamma c\tau}$, where

$$c\tau = 0.2 \left(\frac{1 \text{ eV}}{\Gamma_{\text{NLSP}}}\right) \mu\text{m} = 0.2 \left(\frac{1 \text{ } \mu\text{eV}}{\Gamma_{\text{NLSP}}}\right) \text{ m} \tag{4}$$

and $\beta\gamma = (E^2/m_{\text{NLSP}}^2 - 1)^{1/2}$.

The MGM (Minimal Gauge Mediation) is the simplest phenomenological model of gauge mediated SUSY breaking (GMSB). MGM assumes N generations of messenger fields in the $\mathbf{5} \oplus \overline{\mathbf{5}} \in SU(5) \supset SU(3)_C \times SU(2)_L \times U(1)_Y$. The messengers have an overall supersymmetric mass M_m, with the scalar and fermion split by a SUSY breaking auxiliary order parameter F_S with units of [mass]^2. The MSSM gaugino masses arise from a one-loop coupling to the messengers, whereas the MSSM scalar masses arise from a two-loop coupling to the messengers. Both gaugino and sfermion masses are proportional to

$$\Lambda = F_S/M_m \tag{5}$$

The MSSM superpartner masses are evolved from the messenger scale to the electroweak scale by renormalization group evolution. This is the only way in which the messenger scale M_m is entering directly, so the MSSM parameters only depend weakly (logarithmically) on M_m. The MSSM gaugino masses arise from one-loop coupling to the messengers,

$$M_a = k_a N\Lambda \frac{\alpha_a}{4\pi} \tag{6}$$

where $\Lambda = F_S/M_m$ is the effective visible sector SUSY breaking parameter, and $a = 1, 2, 3$ for the Bino, Wino, and gluino respectively, and $k_1 = \frac{5}{3}$, $k_2 = k_3 = 1$.

The MSSM scalar masses arise from a two-loop coupling to the messengers

$$m_\phi^2 = 2N\Lambda^2 \left[\frac{5}{3} \left(\frac{Y}{2} \right)^2 \left(\frac{\alpha_1}{4\pi} \right)^2 + C_2 \left(\frac{\alpha_2}{4\pi} \right)^2 + C_3 \left(\frac{\alpha_3}{4\pi} \right)^2 \right] \tag{7}$$

where Y is the ordinary weak hyper charge normalized as
$Q = T_3 + \frac{1}{2}Y$, $C_2 = \frac{3}{4}$ for weak isodoublet scalars and zero for weak isosinglets, and $C_3 = \frac{4}{3}$ for squarks and zero for other scalars. Note that the gaugino masses scale like N while the scalar masses scale like $\sqrt{N}$.

The effective SUSY breaking order parameter F_S, felt by the messengers is, in general, lower than the ultimate underlying SUSY breaking order parameter F which determines the Goldstino coupling. To account for this a dimensionless factor

$$C_G = \frac{F}{F_S} \tag{8}$$

relating F and F_S may be introduced. With all other MGM parameters fixed, C_G may be used to control the NLSP decay length:

$$c\tau(\widetilde{X} \to X\widetilde{G}) \simeq C_G^2 \left(\frac{1 \text{ m}}{\kappa} \right) \left(\frac{100 \text{ GeV}}{m_{\tilde{X}}} \right)^5 \left(\frac{\sqrt{\Lambda \cdot M_m}}{1000 \text{ TeV}} \right)^4 \left(1 - \frac{m_X^2}{m_{\widetilde{X}}^2} \right)^{-4} \tag{9}$$

This model is useful for phenomenological studies since any given model can be specified in terms of six parameters

$$\Lambda \,,\; N \,,\; M_m \,,\; \tan\beta \,,\; \text{sgn}(\mu) \,,\; C_G \tag{10}$$

The phenomenological meaning and importance of the MGM parameters can be summarized as follows:

- Λ: This effective visible sector SUSY breaking parameter sets the overall mass scale for all the MSSM superpartners. For electroweak scale superpartners $\Lambda \sim \mathcal{O}(100 \text{ TeV})/\sqrt{N}$. In the first approximation, all of the MSSM superpartner masses scale linearly with Λ.

- N: The gaugino masses scale like the number of messenger generations, N, while the squark and slepton masses scale like $\sqrt{N}$. For low values of N a Bino-like neutralino, $\widetilde{\chi}_1^0$, is the NLSP, while for larger values a right-handed slepton, $\widetilde{\ell}_R$, is the NLSP.

- M_m: The messenger scale enters as the scale at which the boundary conditions for renormalization group evolution of the MSSM parameters are imposed. The electroweak scale and all of the sparticle masses depend only on the logarithm of M_m. The lower limit $M_m > \Lambda$ is required in order to avoid color and charge breaking in the messenger sector, and $M_m \lesssim 10^{16}$ GeV to satisfy the defining criterion for low-scale SUSY breaking.

- $\tan\beta$: The ratio of the MSSM Higgs vacuum expectation values is in the range $1.5 \lesssim \tan\beta \lesssim 60$. The lower limit leads to a light CP-even Higgs scalar, with mass close to the LEP limit. Large values of $\tan\beta$ yield a $\tilde{\tau}_1$ slepton which is significantly lighter than the other sleptons.

- $\text{sgn}(\mu)$: The sign of Higgs and Higgsino supersymmetric mass parameter μ appears in the chargino and neutralino mass matrices. For a Higgsino-like neutralino $\widetilde{\chi}_1^0$ NLSP with low to moderate values of $\tan\beta$, $\text{sgn}(\mu)$ is crucial for determining the relative strength of the $\widetilde{\chi}_1^0$ coupling to Higgs and Z bosons through the Goldstino.

- C_G: The ratio of the intrinsic SUSY breaking order parameter F to the messenger sector SUSY breaking order parameter F_S controls the coupling to the Goldstino. The NLSP decay length scales like C_G^2.

2 Neutralino as the Next to Lightest Supersymmetric Particle

The choice of model parameters for the $\widetilde{\chi}_1^0$ analysis chain was motivated by the so called SPS 8 line [3].

$$N = 1 \quad \tan\beta = 1 \quad \text{sgn}\,\mu = 1 \quad M_m = 2\Lambda \tag{11}$$

The dependence of the cross section at the LHC on the scaling parameter Λ and mass of some supersymmetric particles is plotted in Figure 1. In particular it can be seen, that the neutralino $\widetilde{\chi}_1^0$ is indeed lighter than the stau $\tilde{\tau}_1$ in this model.

Figure 1: The GMSB SPS8 line cross section at LHC and masses of a few chosen supersymmetric particles as a function of the scaling parameter Λ.
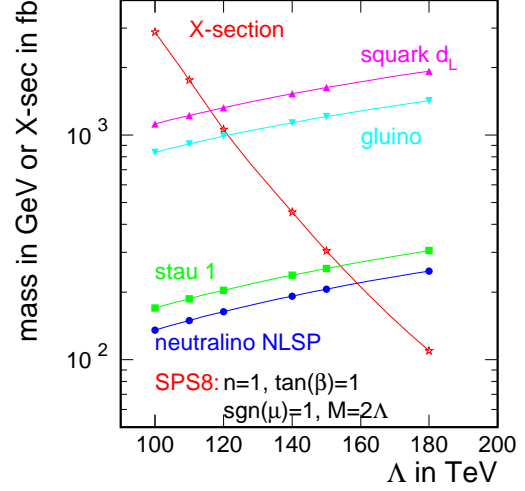
2.1 Signal simulation

For full detector simulation of the $\widetilde{\chi}_1^0$ analysis chain the point $\Lambda = 140\,\text{TeV}$ was chosen from the SPS8 line. Masses of the supersymmetric particles for this point are above the TeVatron reach [2]. Electroweak scale parameters of this point are given in the Table 1.

The main interest of the present analysis of $\widetilde{\chi}_1^0$ NLSP is to verify to what extent its lifetime could be estimated using the electromagnetic calorimeter (ECAL) of the CMS detector. For this purpose several signal datasets with different values of the parameter $c\tau$ of $\widetilde{\chi}_1^0$ were simulated using OSCAR 3.9.8 and ORCA 8.13.1 for digitization and reconstruction.

The characteristics of the signal is the following:

- at least one energetic photon,

- large missing transverse momentum,

- large number of high transverse momentum jets.

For this part of the analysis single photon HLT trigger path was chosen. The transverse momentum threshold is $p_T^\gamma > 80\,\text{GeV}$.

2.2 Background

All multijet background sources were considered

1. inclusive Z plus jets

2. inclusive W plus jets

3. inclusive multi jet QCD

4. inclusive $t\bar{t}$ plus jets

5. inclusive WW plus jets

6. inclusive ZW plus jets

7. inclusive ZZ plus jets

The single photon trigger already reduces the background because an isolated photon candidate with transverse momentum above 80 GeVis required. However multi jet background contains QED photons and pathological jets with leading π^0 that could mimic isolated photons.

Table 1: Electroweak scale parameters used by PYTHIA for point $\Lambda = 140 \text{TeV}$ of the SPS8 GMSB line,

```
**************** PYSLHA v1.02: SUSY SPECTRUM INTERFACE ****************
*    PYSLHA: Last Change 29 Apr 2004 - P.Z. Skands
*    Spectrum Calculator was: ISASUGRA   # version ISAJET    V
*    Read spectrum file on unit:  33
*
* EW scale masses:
*        ~d       ~u       ~s       ~c     ~b(12)   ~t(12)
*  L  1527.75  1525.63  1527.75  1525.63  1446.82  1332.32
*  R  1453.41  1459.50  1453.41  1459.50  1467.15  1480.28
*
*        ~e      ~nu_e      ~mu    ~nu_mu  ~tau(12)  ~nu_tau
*  L   502.62   489.86   502.62   489.86   237.68   488.96
*  R   245.42     0.00   245.42     0.00   502.38     0.00
*
*        ~g    ~chi_10  ~chi_20  ~chi_30  ~chi_40  ~chi_1+  ~chi_2+
*    1135.72   191.69   377.86   561.27   577.86   378.36   577.78
*
*   ~gravitino
*    5.67739391E-07
*
*        h0       H0       A0       H+
*      116.99   730.16   725.27   734.59
*
* Mixing structure:
*          |   ~B   |   ~W_3  |   ~H_1  |   ~H_2  |
*   ~chi_10 |  0.995 | -0.018  |  0.091  | -0.038  |
*   ~chi_20 | -0.046 | -0.956  |  0.238  | -0.166  |
*   ~chi_30 |  0.037 | -0.054  | -0.703  | -0.708  |
*   ~chi_40 | -0.082 |  0.288  |  0.664  | -0.685  |
*
*      L   |   ~W   |   ~H   |            R    |   ~W   |   ~H   |
*   ~chi_1+ | -0.936 |  0.353 |       ~chi_1+ | -0.970 |  0.245 |
*   ~chi_2+ | -0.353 | -0.936 |       ~chi_2+ | -0.245 | -0.970 |
*
*      |  ~b_L  |  ~b_R  |       |  ~t_L  |  ~t_R  |          | ~tau_L | ~tau_R |
*   ~b_1 |  0.315 | -0.949 |  ~t_1 |  0.106 | -0.994 |   ~tau_1 |  0.070 | -0.998 |
*   ~b_2 |  0.949 |  0.315 |  ~t_2 |  0.994 |  0.106 |   ~tau_2 |  0.998 |  0.070 |
*
* Couplings:
*    A_b =  -440.44          A_t =  -393.82    A_tau =   -52.86
*   alpha =    1.00    tan(beta) =    1.00        mu =   552.95
*
***************************** END OF PYSLHA *****************************
```
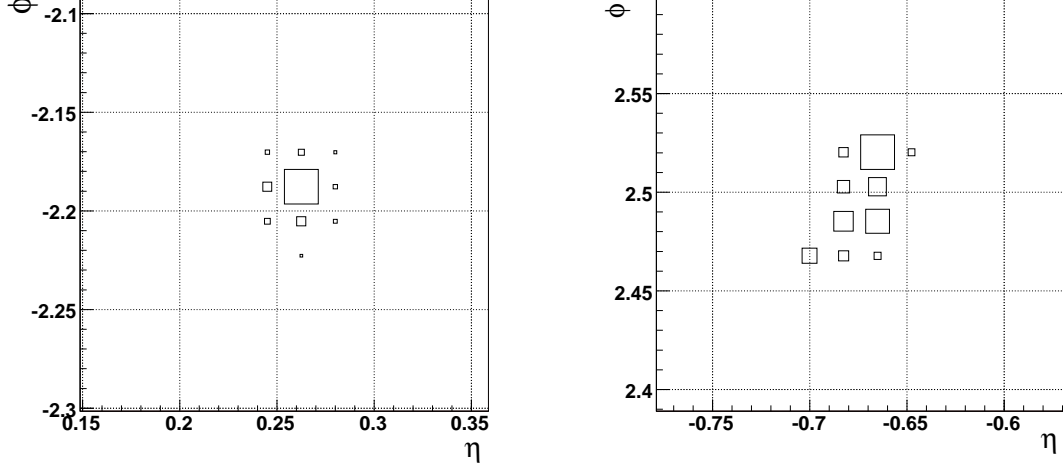
Figure 2: Energy distribution among ECAL crystals for a (left) pointing and (right) non-pointing photon.

2.3 Offline selection

Most of the supersymmetric events originate from squark and gluino production. Each cascade decay of a heavy supersymmetric event ends with the $\widetilde{\chi}_1^0 \to \tilde{G}\gamma$ decay. In the present analysis we are looking for events in which at least one $\widetilde{\chi}_1^0$ decays before crossing ECAL. We require at least one photon, at least four hard jets and large missing transverse momentum.

Consequently, the following selection procedure was used to suppress background on top of the HLT requirement.

1. Transverse momentum of the most energetic gamma: $p_T^{1\gamma} > 80 \text{GeV}$.
   The value of this cut is motivated by the trigger threshold, and an observation, that electromagnetic deposit of an isolated π^0 having lower transverse momentum could mimic the signature of non-pointing photon [4].

2. Photon isolation: less than 3 GeV of the algebraic sum of transverse momenta of charged tracks in the (η, ϕ) cone of 0.3 around the photon candidate.

3. Pseudorapidity of the jet with the highest transverse momentum: $|\eta^{1j}| < 1.7$.

4. The minimum of ϕ angle differences between p_T^{miss} and one of the four jets with the highest transverse momentum: $\phi_{\min} > 20°$.
   This cut suppresses background events in which a large p_T^{miss} is due to mismeasurement of one of the jets.

5. Transverse momentum of the jet with fourth highest transverse momentum: $p_T^{4j} > 50 \text{GeV}$

6. Missing transverse momentum: $p_T^{\text{miss}} > 160 \text{GeV}$

2.4 Non-pointing photon signature

Photons from the $\widetilde{\chi}_1^0 \to \tilde{G}\gamma$ decay could be reconstructed as non-pointing to the interaction point if $c\tau$ is greater than $\mathcal{O}(10\text{cm})$. The energy of a non-pointing photon is distributed along many ECAL crystals and forms an ellipse which major axis agrees with the intersection between (i) the plane determined by the $\widetilde{\chi}_1^0$ and photon directions and (ii) the ECAL cylinder. The asymmetry of this ellipse is correlated to the angle between the $\widetilde{\chi}_1^0$ and photon directions.

An example energy distribution among ECAL crystals for pointing and non-pointing photons is shown in Figure 2.

The above observation leads to the following quantitative description of the non-pointing photon signature [4]. The spatial distribution of the energy deposit in the ECAL could be characterized by the covariance matrix

$$COV_{\phi\eta} = \begin{pmatrix} S_{\phi\phi} & S_{\phi\eta} \\ S_{\phi\eta} & S_{\eta\eta} \end{pmatrix},$$ \hfill (12)

6

where:

$$S_{\mu\nu} = \frac{1}{E_\gamma} \sum_{i=1}^{N} E_i \cdot (\mu_i - \langle\mu\rangle)(\nu_i - \langle\nu\rangle) \tag{13}$$

and where N is the number of crystals associated to the photon candidate; $\mu, \nu = \phi, \eta$; E_i $(i = 1, N)$ is the energy deposited in the crystal i; $E_\gamma = \sum_{i=1}^{N} E_i$ and $\langle\mu\rangle = \sum_{i=1}^{N} \mu_i \cdot E_i/E_\gamma$.

The covariance matrix can be diagonalized, which is equivalent to finding the major and minor axes of the energy deposit ellipse

$$\begin{pmatrix} S_{\mathrm{major}} & 0 \\ 0 & S_{\mathrm{minor}} \end{pmatrix} = \begin{pmatrix} \frac{S_{\phi\phi}+S_{\eta\eta}+\sqrt{(S_{\phi\phi}-S_{\eta\eta})^2+4S_{\phi\eta}^2}}{2} & 0 \\ 0 & \frac{S_{\phi\phi}+S_{\eta\eta}-\sqrt{(S_{\phi\phi}-S_{\eta\eta})^2+4S_{\phi\eta}^2}}{2} \end{pmatrix} \tag{14}$$

The energy deposit can be characterized by three quantities:

1. the RMS of energy distribution along major axis

$$\sqrt{S_{\mathrm{major}}} = \sqrt{\frac{S_{\phi\phi} + S_{\eta\eta} + \sqrt{(S_{\phi\phi} - S_{\eta\eta})^2 + 4S_{\phi\eta}^2}}{2}} \tag{15}$$

2. the asymmetry Δ

$$\Delta = \frac{S_{\mathrm{major}} - S_{\mathrm{minor}}}{S_{\mathrm{major}} + S_{\mathrm{minor}}} = \frac{\sqrt{(S_{\phi\phi} - S_{\eta\eta})^2 + 4S_{\phi\eta}^2}}{S_{\phi\phi} + S_{\eta\eta}} \tag{16}$$

3. the angle α between the major axis and local ϕ coordinate

$$\alpha = \arctan\left(\frac{S_{\eta\eta} - S_{\phi\phi} + \sqrt{(S_{\phi\phi} - S_{\eta\eta})^2 + 4S_{\phi\eta}^2}}{2S_{\phi\eta}}\right) \tag{17}$$

A scatter plot Δ versus α is shown in Figure 3 for $c\tau = 100$ cm and $c\tau = 0$. As expected, the asymmetry is large for large $c\tau$ and small for $c\tau = 0$. However, for $\alpha \approx 0$ and $|\alpha| \approx \pi/2$, even in the second case a large asymmetry is observed. The reason for this is twofold. Significant asymmetry in the case when the major axis is aligned with the local ϕ direction is due to photon conversion into an e^+e^- pair in the tracker. The CMS magnetic field bends the electrons and in the ECAL they have different ϕ but not different η. The second reason is a purely geometric effect due to ECAL granulation. Spatial distribution of the ECAL energy deposit for a pointing photon is, approximatively, a two dimensional Gaussian, with an RMS of the order of crystal width. The distribution of the energy deposits in the crystals can have a center of symmetry only if the center of the Gaussian is close to the center of one of the crystals or close to the junction of four crystals. In the all other cases the distribution will have two axes of symmetry along local ϕ and η directions and major axis will be close to one of these axes.

In consequence the asymmetry Δ contains viable information only in the α *signal region* which we define to be

$$0.2 < |\alpha| < 1.35 \tag{18}$$

For the purpose of $\widetilde{\chi}_1^0$ lifetime estimation and signal significance determination the selected photons were divided into $3 \times 2 \times 3 \times 2 = 36$ separate groups by binning the following observables:

- $\begin{array}{lll} j = 1 & & \Delta < 1/3 \\ j = 2 & 1/3 < & \Delta < 2/3 \\ j = 3 & 2/3 < & \Delta \end{array}$

- $\begin{array}{lll} k = 1 & 80\,\mathrm{GeV} < & p_T^{1\gamma} < 200\,\mathrm{GeV} \\ k = 2 & 200\,\mathrm{GeV} < & p_T^{1\gamma} \end{array}$

- $\begin{array}{lll} l = 1 & 0.2 < & |\alpha| < 1.35 \\ l = 2 & & |\alpha| > 1.35 \\ l = 3 & 0.2 > & |\alpha| \end{array}$
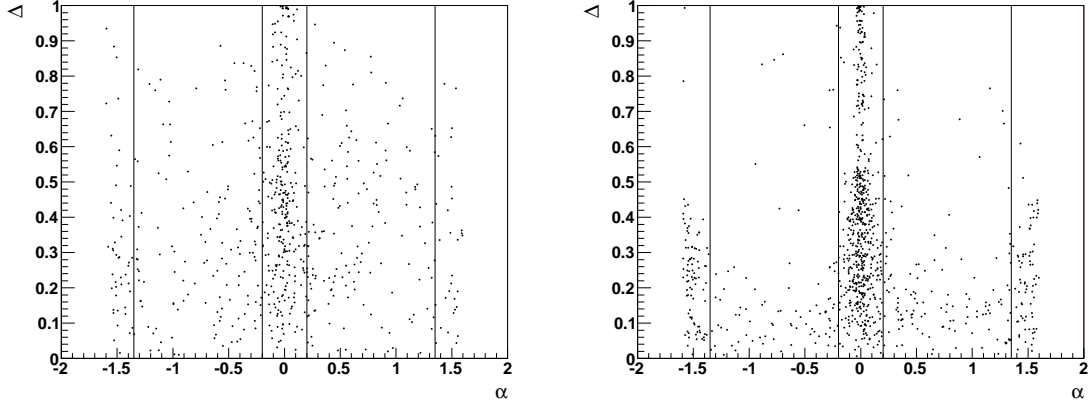
Figure 3: Scatter plot Δ versus α for (left) $c\tau$=100cm and (right) $c\tau = 0$

- $\begin{aligned} m &= 1 \quad 220\,\mathrm{GeV} < p_T^{\mathrm{miss}} \quad \& \quad 60\,\mathrm{GeV} < p_T^{4j} \\ m &= 2 \quad 160\,\mathrm{GeV} < p_T^{\mathrm{miss}} \quad \& \quad 50\,\mathrm{GeV} < p_T^{4j} \quad \& \quad \mathbf{not}(m = 1) \end{aligned}$

Each group is defined by a set o requiremnts $\{j, k, l, m\}$.

The full set of groups defined above was used for the lifetime determination, as described in Section 2.7. For the estimation signal significance, however, only two regions were used:

- Non-pointing signal region (sel-I): $\{j = 2, 3; k = 1, 2; l = 1; m = 1, 2\} \cup \{j = 3; k = 1, 2; l = 2, m = 1, 2\}$ which is equivalent to select $\Delta > 1/3$ in α signal region and $\Delta > 2/3$ for $|\alpha| > 1.35$.

- Pointing photon in a hard event (sel-II): $\{j = 1; k = 1, 2; l = 1, 2, 3; m = 1\} \cup \{j = 2; k = 1, 2; l = 2, 3; m = 1\} \cup \{j = 3; k = 1, 2; l = 3; m = 1\}$. This corresponds to the α and Δ region unselected above and adds harder cut on p_T^{4j} and p_T^{miss}.

The distributions of the quantities used in the selection described in Section 2.3 (after all cuts but the cut on the plotted quantity) are shown in Figure 4 for pointing photon selection (sel-II) for signal with $c\tau = 0$ and in Figure 5 for non-pointing photon selection (sel-I) for signal with $c\tau = 100\,\mathrm{cm}$. Effective mass $M_{\mathrm{eff}} = \sum_{j=1}^{4} p_T^j + p_T^{\mathrm{miss}}$ plots after (i) HLT selection and cut on $p_T^{1\gamma} > 80\mathrm{GeV}$ and (ii) after final selection are shown in Figure 6.

The number of expected events at different stages of the selection procedure is given in Table 2.

2.5 Systematic uncertainty

Numbers in columns marked "+syst." in Table 2 are obtained after taking into account the following systematic uncertainties:

- The positive systematic uncertainty on p_T^{miss} due to tails in the jet energy resolution was estimated (on the basis of a study described in [6]) to be 7% above 180GeV [5].

- Jet energy scale is expected to be uncertain at the level of $\delta p_T^{4j} = 3\%$ after taking 10/fb data [7]. We take this value as the estimate of the p_T^{4j} positive uncertainty.

- Photon energy resolution is expected to be $\delta p_T^{1\gamma} = 0.5\%$ at $p_T^{1\gamma} = 80\mathrm{GeV}$ [8]. We take this value also as positive uncertainty.

An important source of systematic effects could be related to an uncertainty in the shape of the background distributions used in the selection process. This problem is common to all inclusive selections of supersymmetry and cannot be resolved before LHC startup. Because of that, the signal significance evaluated in the next section is valid only if these shapes are correctly described at generator level in the background datasets used. Several methods of determination of the background level directly from data were developed by CMS collaboration. For details see reference [10].
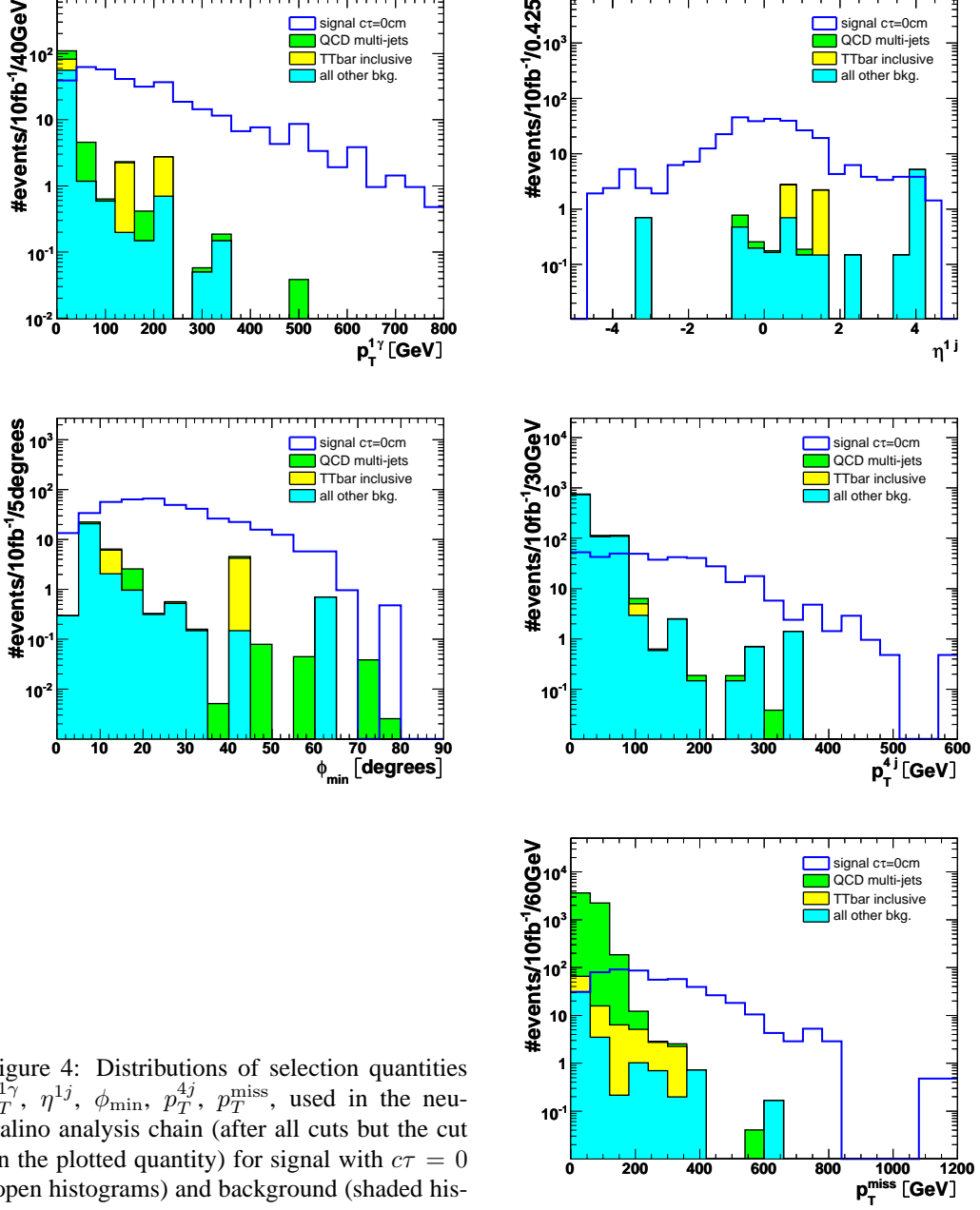
Figure 4: Distributions of selection quantities $p_T^{1\gamma}$, η^{1j}, $\phi_{\min}$, p_T^{4j}, p_T^{miss}, used in the neutralino analysis chain (after all cuts but the cut on the plotted quantity) for signal with $c\tau = 0$ (open histograms) and background (shaded histograms).
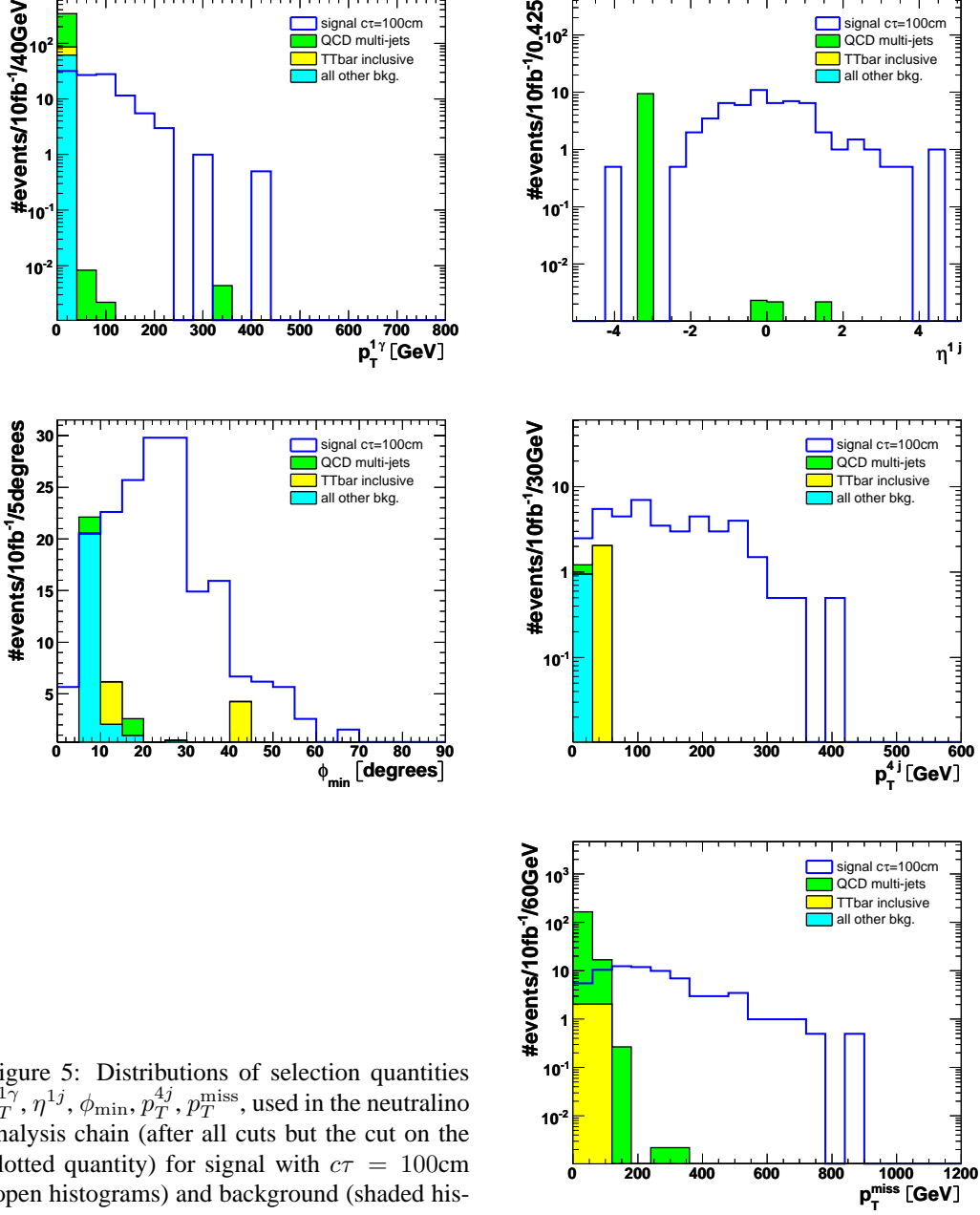
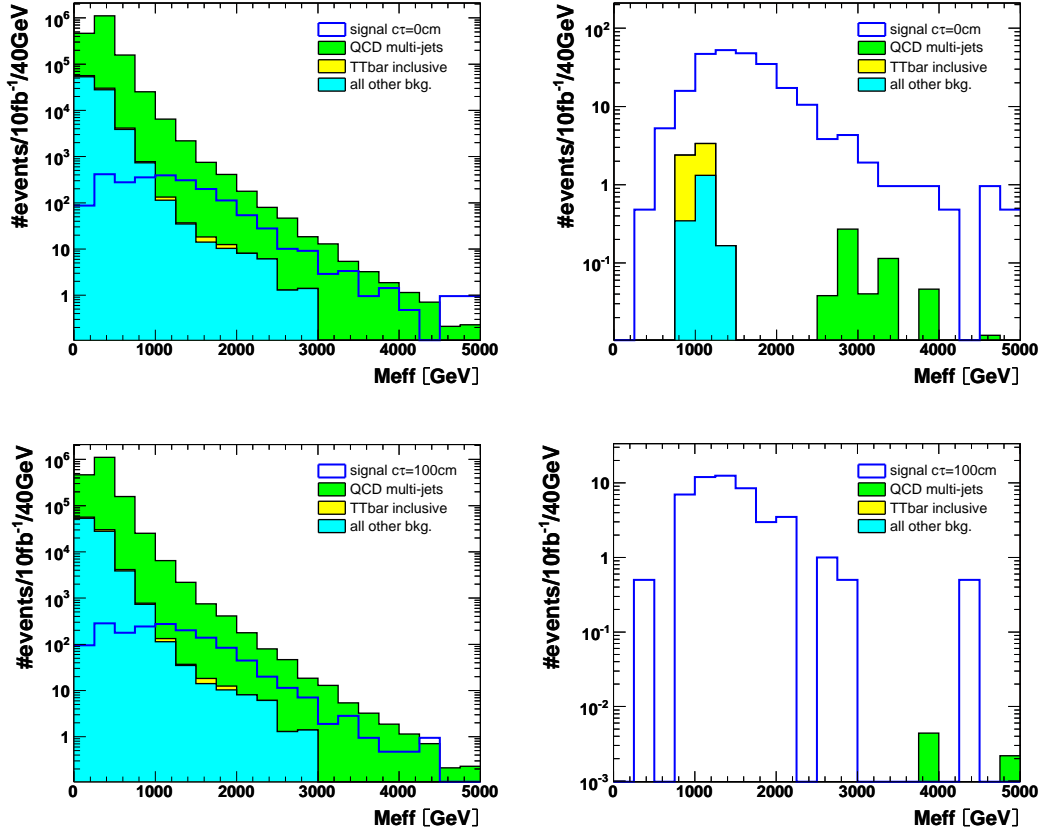Figure 5: Distributions of selection quantities $p_T^{1\gamma}$, η^{1j}, $\phi_{\min}$, p_T^{4j}, p_T^{miss}, used in the neutralino analysis chain (after all cuts but the cut on the plotted quantity) for signal with $c\tau = 100$cm (open histograms) and background (shaded histograms).

Figure 6: Distribution of M_{eff} after HLT selection and cut on $p_T^{1\gamma} > 80\,\mathrm{GeV}$ (left) and after final selection (right) for $c\tau = 0\,\mathrm{cm}$ (top) and for $c\tau = 100\,\mathrm{cm}$ (bottom).

Table 2: The number of expected events at different stages of the selection procedure for an integrated luminosity of $\mathcal{L} = 10/fb$. The meaning of column titles is the following: dataset – self explanatory; # – number of simulated events; X-sec – cross section in femtobarns; cut1 – number of events left after HLT and $p_T^{1\gamma}$ requirements; cut2 – after η and ϕ requiremnts; cut3 – after the full selection described in Section 2.3; sel-I – nonpointing signal region; sel-II – pointing signal region.

| dataset	#	X-sec	cut1	cut2	cut3	sel-I	+syst.	sel-II	+syst.
su05_L140_M280_ct1	9181.	0.45E+00	2104.28	783.24	402.98	2.96	2.96	262.23	289.39
su05_L140_M280_ct250	9379.	0.45E+00	2061.69	763.24	379.71	28.14	29.10	219.43	243.76
su05_L140_M280_ct500	6783.	0.46E+00	1948.33	718.48	361.60	41.15	45.87	194.97	215.88
su05_L140_M280_ct1000	9068.	0.47E+00	1564.12	601.39	298.12	50.89	56.03	167.57	182.99
su05_L140_M280_ct2000	9074.	0.46E+00	1037.60	364.94	166.66	34.13	34.64	92.87	99.39
su05_L140_M280_ct4000	8742.	0.45E+00	645.77	229.28	114.89	25.13	26.16	63.09	67.19
jm03b_Zjets_50_85	184000.	0.15E+04	1107.82	158.19	0.00	0.00	0.00	0.00	0.00
jm03b_Zjets_85_150	276000.	0.58E+03	2276.44	396.79	0.00	0.00	0.00	0.00	0.00
jm03b_Zjets_150_250	128000.	0.16E+03	1528.80	214.78	0.00	0.00	0.00	0.00	0.00
jm03b_Zjets_250_400	92000.	0.37E+02	895.76	151.28	0.00	0.00	0.00	0.00	0.00
jm03b_Zjets_400_700	44000.	0.70E+01	277.34	57.05	0.00	0.00	0.00	0.00	0.00
jm03b_Zjets_700_1100	26000.	0.71E+00	45.27	12.89	0.55	0.00	0.00	0.27	0.27
jm03b_Zjets_1100_1600	19500.	0.85E-01	5.71	1.53	0.09	0.00	0.00	0.09	0.09
jm03b_Zjets_1600_2200	19500.	0.12E-01	0.79	0.21	0.01	0.00	0.00	0.01	0.01
ΣZjets		0.22E+04	6137.93	992.73	0.65	0.00	0.00	0.37	0.37
jm03b_Wjets_85_150	464000.	0.43E+04	3063.05	371.20	0.00	0.00	0.00	0.00	0.00
jm03b_Wjets_150_250	152000.	0.12E+04	2927.01	79.03	0.00	0.00	0.00	0.00	0.00
jm03b_Wjets_250_400	156000.	0.26E+03	1552.46	151.86	0.00	0.00	0.00	0.00	0.00
jm03b_Wjets_400_700	94000.	0.49E+02	602.99	93.56	0.00	0.00	0.00	0.00	0.00
jm03b_Wjets_700_1100	70000.	0.49E+01	126.45	26.55	1.40	0.00	0.00	0.70	0.70
jm03b_Wjets_1100_1600	40000.	0.59E+00	24.84	6.21	1.03	0.00	0.00	0.59	0.59
jm03b_Wjets_1600_2200	5000.	0.83E-01	5.13	0.99	0.33	0.00	0.00	0.17	0.17
ΣWjets		0.58E+04	8301.93	729.40	2.76	0.00	0.00	1.46	1.46
jm03b_qcd_170_230	338000.	0.10E+06	445213.47	59757.61	0.00	0.00	0.00	0.00	0.00
jm03b_qcd_230_300	236000.	0.24E+05	194078.34	23248.08	0.00	0.00	0.00	0.00	0.00
jm03b_qcd_300_380	144000.	0.64E+04	85657.78	15089.61	0.00	0.00	0.00	0.00	0.00
jm03b_qcd_380_470	186000.	0.19E+04	37082.08	9956.21	0.00	0.00	0.00	0.00	0.00
jm03b_qcd_470_600	186000.	0.69E+03	17182.54	4750.22	37.07	0.00	0.00	0.00	0.00
jm03b_qcd_600_800	84000.	0.20E+03	6292.06	2483.06	0.00	0.00	0.00	0.00	0.00
jm03b_qcd_800_1000	38000.	0.36E+02	1551.67	686.49	0.00	0.00	0.00	0.00	0.00
jm03b_qcd_1000_1400	80000.	0.11E+02	652.51	339.14	13.56	0.00	0.00	0.00	1.36
jm03b_qcd_1400_1800	40000.	0.11E+01	71.54	40.39	3.17	0.00	0.26	0.26	0.53
jm03b_qcd_1800_2200	38000.	0.14E+00	12.42	7.96	0.84	0.00	0.00	0.23	0.34
jm03b_qcd_2200_2600	40000.	0.24E-01	2.15	1.43	0.18	0.00	0.00	0.03	0.06
jm03b_qcd_2600_3000	19594.	0.43E-02	0.46	0.33	0.06	0.01	0.01	0.02	0.03
jm03b_qcd_3000_3500	23662.	0.84E-03	0.10	0.06	0.01	0.00	0.00	0.01	0.01
jm03b_qcd_3500_4000	8000.	0.97E-04	0.01	0.01	0.00	0.00	0.00	0.00	0.00
ΣQCD		0.13E+06	787797.19	116360.59	54.90	0.01	0.27	0.55	2.32
jm03b_ZZjets_inclusive	360849.	0.11E+02	11.08	0.62	0.00	0.00	0.00	0.00	0.00
jm03b_WWjets_inclusive	334511.	0.19E+03	803.85	61.83	0.00	0.00	0.00	0.00	0.00
jm03b_ZWjets_inclusive	175575.	0.27E+02	21.42	4.59	0.00	0.00	0.00	0.00	0.00
jm03b_TTbar_inclusive	2408979.	0.49E+03	4662.89	884.37	16.34	0.00	0.00	4.08	6.13
Σtotal		0.14E+06	807736.31	119034.12	74.65	0.01	0.27	6.46	10.27
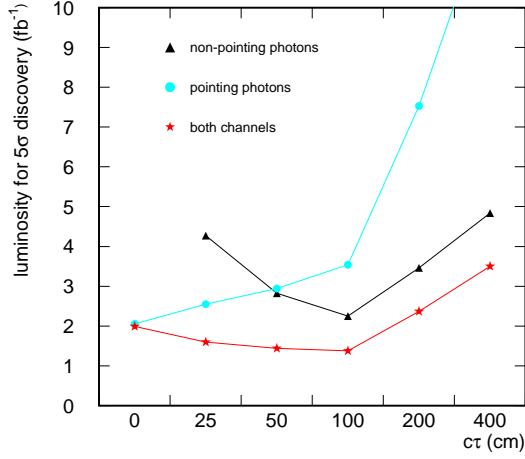
Figure 7: An integrated luminosity necessary for 5σ discovery in function of $c\tau$ (triangles: the non-pointing signal region (sel-I), circles: pointing signal region (sel-II) and stars for a sum of both channels).
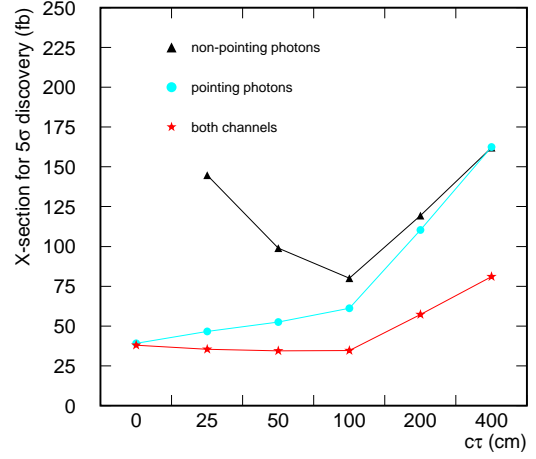
Figure 8: A cross section necessary for 5σ discovery in function of $c\tau$ (triangles: the non-pointing signal region (sel-I), circles: pointing signal region (sel-II) and stars for a sum of both channels).

2.6 Signal significance

Signal significance is calculated using the formula [10]:

$$S_{c12s} = 2 \cdot \left(\sqrt{s+b} - \sqrt{b} \right) \frac{b}{b + \Delta b^2} \tag{19}$$

and using the numbers given in Table 2. In Figure 7 the estimate of a minimal amount of integrated luminosity needed for a 5σ discovery for a given simulated $c\tau$ values is given. The triangles are plotted for the non-pointing signal region (sel-I), circles for pointing signal region (sel-II) and stars for the sum of both channels (lines are drown only to guide the eye).

The behavior of significance shown in Figure 7 could be understood in the following way. With growing lifetime the probability for the $\widetilde{\chi}_1^0$ to decay before crossing ECAL diminishes. In the same time the probability for observing a non-pointing signature is growing. Because of that significance due to pointing photons decreases slowly up to $c\tau = 100\,\mathrm{cm}$ and much faster for greater lifetimes, whereas the significance maximum for the non-pointing photons signature is around $c\tau = 100\mathrm{cm}$.

Finally, an integrated luminosity $\mathcal{L} = 2/\mathrm{fb}$ is sufficient to claim discovery for $c\tau \leq 100\mathrm{cm}$ and $\mathcal{L} = 3.5/\mathrm{fb}$ for $c\tau \leq 400\mathrm{cm}$.

In Figure 8 the minimal overall signal cross section for 5σ discovery for an integrated luminosity of $\mathcal{L} = 10/\mathrm{fb}$ is plotted (supposing that changes in the cross section do not change the signal efficiencies). Because a cross section of less than 100 fb is sufficient even in the worst case of $c\tau = 400\mathrm{cm}$, it could be stated that models with $\Lambda = 180\mathrm{TeV}$ from the SPS 8 line (see Fig. 1) could be discovered with an integrated luminosity of $\mathcal{L} = 10/\mathrm{fb}$.

2.7 Neutralino lifetime determination

The most interesting aspect of the present analysis is a determination of the $\widetilde{\chi}_1^0$ lifetime. Prior to such an endeavor it is necessary to know, at least approximately, which point of GMSB parameter space Nature has chosen.

However, even if our knowledge is minimal, the determination will not be completely hopeless, because the quantities that can be used for the lifetime determination depend only weakly on the properties of a specific GMSB point. Nevertheless, we examine in this section the feasibility of a lifetime determination supposing that the $\widetilde{\chi}_1^0$ $c\tau$ is the only unknown GMSB parameter.

The probability that a photon from $\widetilde{\chi}_1^0$ decay will be seen in the ECAL increases with decreasing $\widetilde{\chi}_1^0$ momentum because of relativistic time dilation.

Hence, the information about the lifetime is encoded in a two dimensional distribution $(\Delta, p_T^{1\gamma})$. Residual information comes from the ratio of the number of photons in the α *signal region* (Eq. 17) to the total number of photons.

In Figure 9 the distributions of $p_T^{1\gamma}$ after the selection described in Section 2.3 and the asymmetry Δ (after an additional requirement $0.2 < |\alpha| < 1.35$) are plotted, for signals with different $c\tau$ values and for the background.

$c\tau$ values of the simulated datasets forming a geometric series $25\,\mathrm{cm}, 50\,\mathrm{cm}\,...\,400\,\mathrm{cm}$ were chosen for the analysis. These samples were labeled by

$$i = \begin{cases} 0 & \text{for } c\tau = 0 \\ 1 + \log_2 \frac{c\tau}{12.5\,\mathrm{cm}} & \text{for } c\tau > 0 \end{cases} \tag{20}$$

for the purpose of the $\widetilde{\chi}_1^0$ $c\tau$ determination procedure. It can be observed, that mean values of the distributions shown in Figure 9 scale linearly with the number i in the first approximation. This means, that the analysis is sensitive to the logarithm of $c\tau/\mathrm{length\_unit}$, rather than to $c\tau$ itself. It means also, that it is not possible to distinguish $c\tau$ values much smaller than $25\,\mathrm{cm}$.

To evaluate the precision with which the $\widetilde{\chi}_1^0$ lifetime could be determined, the following method was used. We want to simulate the situation in which we do not know the value of $\widetilde{\chi}_1^0$ $c\tau$. For this purpose, to the distribution consisting of a signal with a given $c\tau$ S_i, $(i = 2, 4)$ and background B we fit signals with neighboring $c\tau$ values S_{i-1}, S_{i+1} and background B. This way, we test the following composition

$$S_i^{\mathrm{data}} + B^{\mathrm{data}} = p_b \cdot B^{\mathrm{ref.}} + p_s \cdot (f \cdot S_{i-1}^{\mathrm{ref.}} + (1-f) \cdot S_{i+1}^{\mathrm{ref.}}, \tag{21}$$

where: p_b is a ratio of the number of background events estimated to that number in the reference sample, f is an estimate of the fraction $S_{i-1}/(S_{i-1} + S_{i+1})$ and p_s is the ratio of the estimated number of signal events to that number in the reference sample (constructed using the fraction f).

To exploit the above scenario, the statistical bootstrap approach was used. Several pseudo-data samples, corresponding to the luminosity of $10/\mathrm{fb}$ (about half of the available signal statistics) were randomly selected from the total samples of signal and background and then all possible data-reference combinations were used.

The final result is obtained by a linear interpolation

$$i_{\mathrm{fit}} = f \cdot (i-1) + (1-f) \cdot (i+1) = i + 1 - 2f. \tag{22}$$

The error of this interpolation is

$$\delta i_{\mathrm{fit}} = 2 \cdot \delta f \tag{23}$$

where δf is the RMS of the f distribution. The distributions of the fit parameters $p_0, i_{\mathrm{fit}}, p_s$ obtained from the above method are shown in Figure 10. Finally, a 1σ confidence interval for $c\tau$ is

$$c\tau_i \in \left(2^{i_{\mathrm{fit}} - \delta i_{\mathrm{fit}}}, 2^{i_{\mathrm{fit}} + \delta i_{\mathrm{fit}}}\right) 12.5\,\mathrm{cm}. \tag{24}$$

This result is shown in Figure 11.

From this analysis it follows that for an integrated luminosity of $\mathcal{L} = 10/\mathrm{fb}$ the $\widetilde{\chi}_1^0$ lifetime parameter $c\tau$ could be determined at least in the range $\mathcal{O}(10\mathrm{cm})$ to $\mathcal{O}(2\mathrm{m})$ with a relative precision ranging from $^{+15\%}_{-13\%}$ to $^{+32\%}_{-24\%}$.
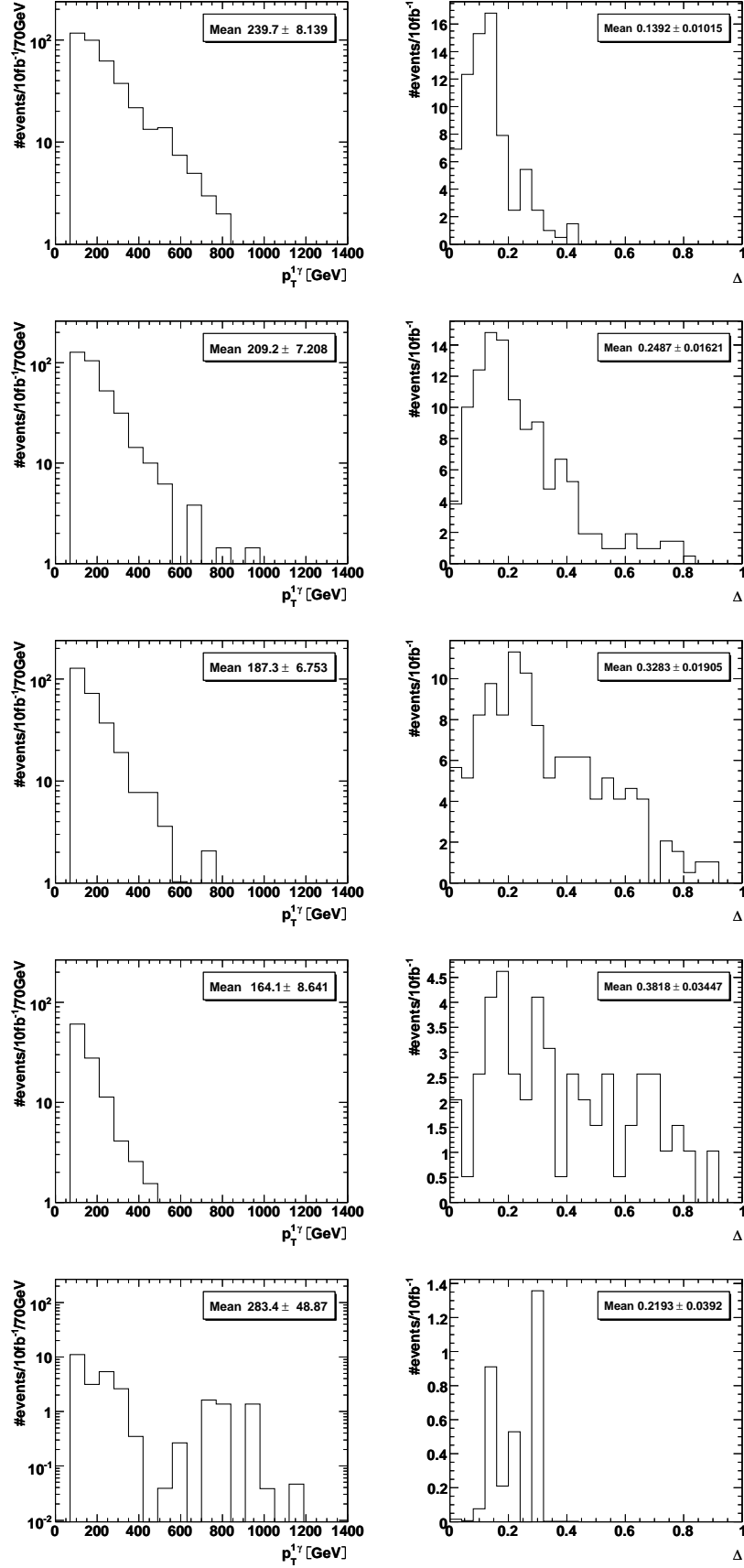
Figure 9: Distributions of $p_T^{1\gamma}$ after the selection described in Section 2.3 (left column) and the asymmetry Δ (after an additional requirement $0.2 < |\alpha| < 1.35$) (right column) for: $c\tau=0$ (row 1); $c\tau=25$ cm (row 2); $c\tau=100$ cm (row 3); $c\tau=400$ cm (row 4); background (row 5).
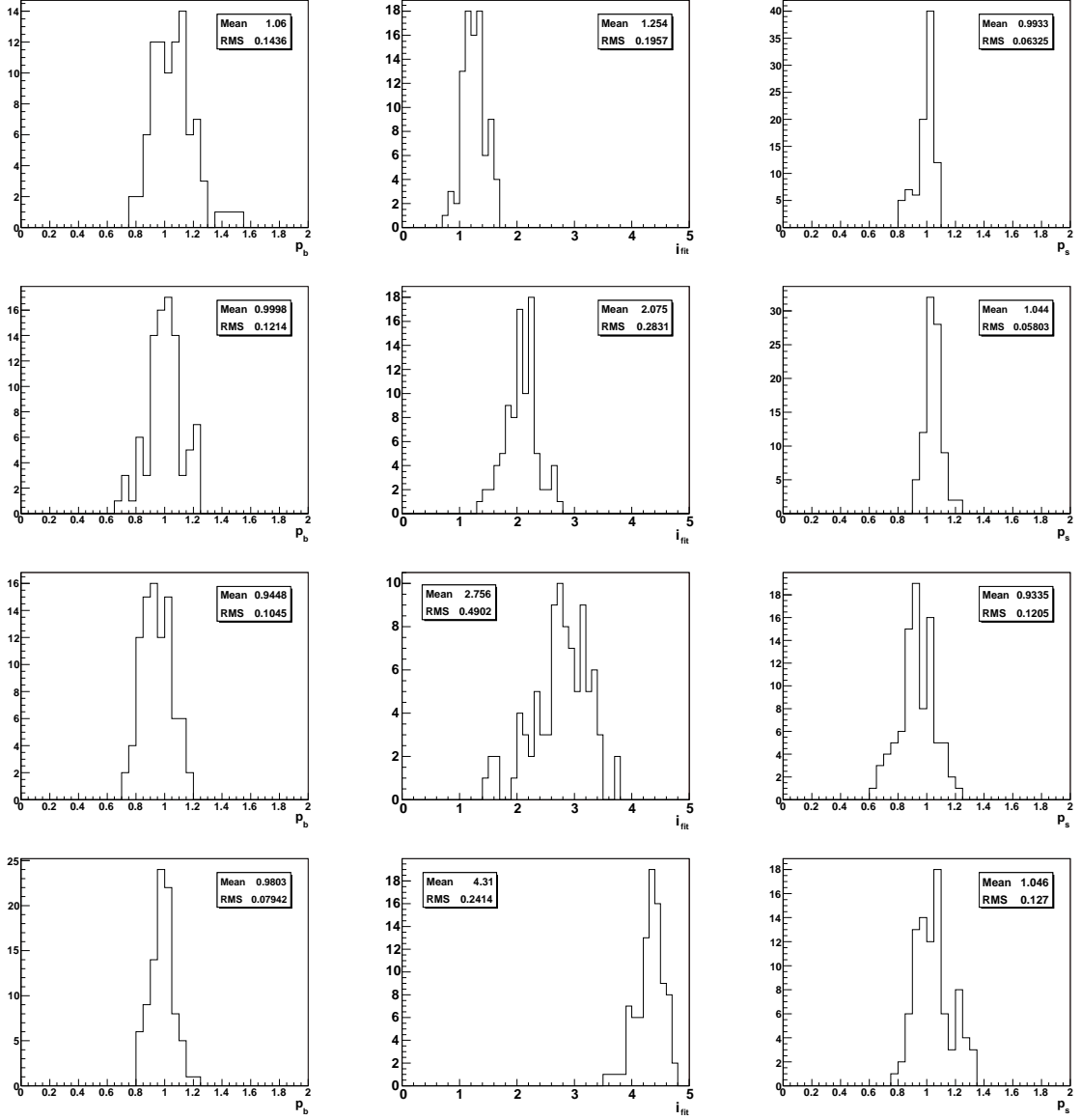
15

Figure 10: Distributions of fit results for the bootstrap method used to evaluate the precision of $\widetilde{\chi}_1^0$ lifetime determination: p_b (column 1); f (column 2); p_s (column 3); row 1: $c\tau$=25 cm ($i = 1$); row 2: $c\tau$=50 cm ($i = 2$); row 3: $c\tau$=100 cm ($i = 3$); row 4: $c\tau$=200 cm ($i = 4$);
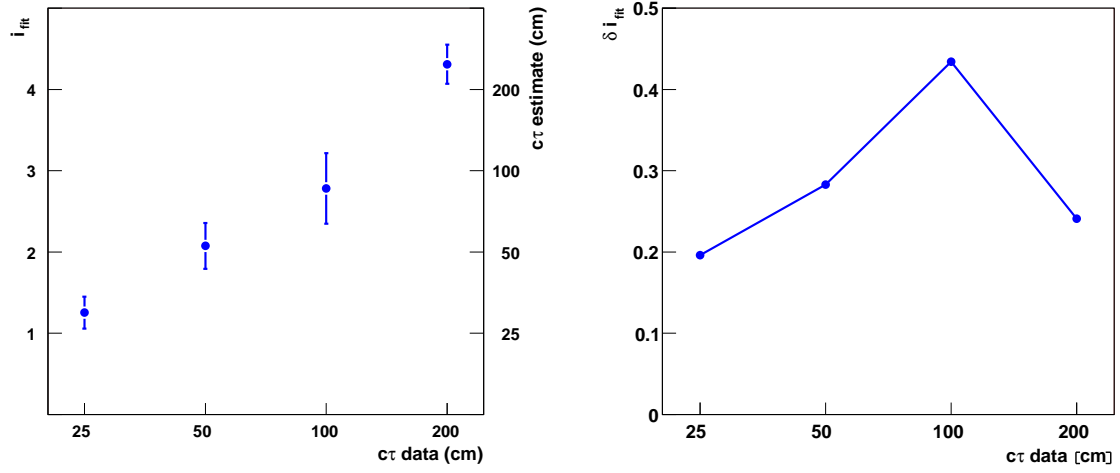
Figure 11: Estimated $\widetilde{\chi}_1^0$ $c\tau$ (i_{fit}) versus input $c\tau$ (left) and $c\tau$ uncertainty δi_{fit} versus input $c\tau$ (right).

Figure 12: The GMSB SPS7 line cross section at the LHC and masses of a few chosen supersymmetric particles as a function of the scaling parameter Λ.
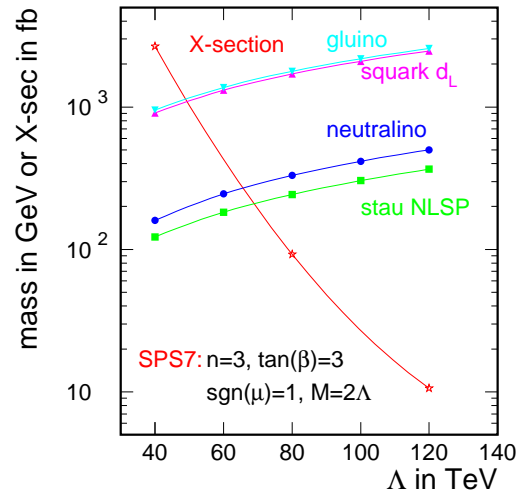
Table 3: Electroweak scale parameters used by PYTHIA at point $\Lambda = 50\,\mathrm{TeV}$ of the SPS7 GMSB line

```
***************** PYSLHA v1.02: SUSY SPECTRUM INTERFACE *****************
*   PYSLHA: Last Change 29 Apr 2004 - P.Z. Skands
*   Spectrum Calculator was: ISASUGRA   # version ISAJET      V
*   Read spectrum file on unit:  33
*
* EW scale masses:
*        ~d        ~u        ~s        ~c     ~b(12)    ~t(12)
*  L  1111.46   1108.37   1111.46   1108.37   1060.72    993.31
*  R  1067.80   1070.33   1067.80   1070.33   1073.82   1091.16
*
*        ~e      ~nu_e       ~mu    ~nu_mu   ~tau(12)   ~nu_tau
*  L   331.37    317.03    331.37    317.03    152.31    316.50
*  R   158.73      0.00    158.73      0.00    332.01      0.00
*
*        ~g    ~chi_10   ~chi_20   ~chi_30   ~chi_40   ~chi_1+   ~chi_2+
*    1164.34    202.47    341.88    381.24    459.13    343.02    456.07
*
*   ~gravitino
*    1.20281311E-05
*
*        h0        H0        A0        H+
*     115.24    482.61    479.29    489.26
*
* Mixing structure:
*            |   ~B   |  ~W_3  |  ~H_1  |  ~H_2  |
*   ~chi_10 |  0.977 | -0.045 |  0.178 | -0.107 |
*   ~chi_20 | -0.189 | -0.601 |  0.573 | -0.523 |
*   ~chi_30 |  0.047 | -0.064 | -0.700 | -0.710 |
*   ~chi_40 |  0.084 | -0.795 | -0.387 |  0.459 |
*
*      L   |   ~W   |   ~H   |              R   |   ~W   |   ~H   |
*   ~chi_1+ | -0.548 |  0.837 |        ~chi_1+ | -0.655 |  0.756 |
*   ~chi_2+ | -0.837 | -0.548 |        ~chi_2+ | -0.756 | -0.655 |
*
*        |  ~b_L  |  ~b_R  |        |  ~t_L  |  ~t_R  |        | ~tau_L | ~tau_R |
*   ~b_1 |  0.480 | -0.877 |   ~t_1 |  0.286 | -0.958 |  ~tau_1 |  0.104 | -0.995 |
*   ~b_2 |  0.877 |  0.480 |   ~t_2 |  0.958 |  0.286 |  ~tau_2 |  0.995 |  0.104 |
*
* Couplings:
*    A_b =  -423.00            A_t =  -383.65    A_tau =    -49.59
*   alpha =     1.00    tan(beta) =      3.00        mu =   373.14
*
***************************** END OF PYSLHA *****************************
```

3   Stau NLSP

The choice of the model parameters for the $\tilde{\tau}_1$ analysis chain was motivated by the so called SPS 7 line [3].

$$N = 3 \quad \tan\beta = 3 \quad \mathrm{sgn}\,\mu = 1 \quad M_m = 2\Lambda \tag{25}$$

The dependence of the LHC cross section and of the masses of a few chosen supersymmetric particles dependence on the scaling parameter Λ are plotted in Figure 12. In particular it can be seen, that the stau $\tilde{\tau}_1$ is indeed lighter than the neutralino $\tilde{\chi}_1^0$ in this model.

3.1   Signal and background simulation

The points $\Lambda = 50\,\mathrm{TeV}$ and $\Lambda = 80\,\mathrm{TeV}$ were chosen for full detector simulation of the $\tilde{\tau}_1$ analysis chain . Masses of the supersymmetric particles for this point are above the TeVatron reach [2]. Electroweak scale parameters of this point are given in the part of PYTHIA output presented in Tables 3 and 4.

The following sources of background were considered:

Table 4: Electroweak scale parameters used by PYTHIA at point $\Lambda = 80\,\mathrm{TeV}$ of the SPS7 GMSB line

```
**************** PYSLHA v1.02: SUSY SPECTRUM INTERFACE ****************
*   PYSLHA: Last Change 29 Apr 2004 - P.Z. Skands
*   Spectrum Calculator was: ISASUGRA   # version ISAJET     V
*   Read spectrum file on unit:  33
*
* EW scale masses:
*        ~d       ~u       ~s       ~c    ~b(12)   ~t(12)
*  L  1707.04  1705.04  1707.04  1705.04  1630.23  1523.80
*  R  1636.26  1641.60  1636.26  1641.60  1648.75  1664.20
*
*        ~e      ~nu_e      ~mu    ~nu_mu  ~tau(12)  ~nu_tau
*  L   523.92   510.83   523.92   510.83   242.93   510.03
*  R   249.91     0.00   249.91     0.00   523.54     0.00
*
*        ~g    ~chi_10  ~chi_20  ~chi_30  ~chi_40  ~chi_1+  ~chi_2+
*     1781.47   330.05   542.23   566.59   688.81   547.63   681.68
*
*    ~gravitino
*     3.07920163E-05
*
*        h0       H0       A0       H+
*     117.95   745.70   740.71   750.04
*
* Mixing structure:
*           |   ~B   |   ~W_3  |   ~H_1  |   ~H_2  |
*    ~chi_10 |  0.988 | -0.022 |  0.127 | -0.082 |
*    ~chi_20 | -0.142 | -0.439 |  0.639 | -0.615 |
*    ~chi_30 |  0.031 | -0.042 | -0.704 | -0.708 |
*    ~chi_40 |  0.044 | -0.897 | -0.283 |  0.336 |
*
*     L    |   ~W   |   ~H   |           R    |   ~W   |   ~H   |
*    ~chi_1+ | -0.408 |  0.913 |         ~chi_1+ | -0.486 |  0.874 |
*    ~chi_2+ | -0.913 | -0.408 |         ~chi_2+ | -0.874 | -0.486 |
*
*         |  ~b_L  |  ~b_R  |        |  ~t_L  |  ~t_R  |          | ~tau_L | ~tau_R |
*    ~b_1 |  0.317 | -0.948 |   ~t_1 |  0.182 | -0.983 |   ~tau_1 |  0.060 | -0.998 |
*    ~b_2 |  0.948 |  0.317 |   ~t_2 |  0.983 |  0.182 |   ~tau_2 |  0.998 |  0.060 |
*
* Couplings:
*     A_b =  -635.80         A_t =  -577.15   A_tau =   -83.83
*   alpha =     1.00   tan(beta) =     3.00       mu =   557.24
*
***************************** END OF PYSLHA ****************************
```

1. Drell-Yan production of muon pairs (above the Z^0 resonance: $\hat{s} > 115\,\text{GeV}$)

2. $t\bar{t}$ with two muons in the final state

3. vector boson pair production with two muons in the final state

The background due to cosmic muon was shown to be negligible (see Sec. 3.6) and was not taken into account in the detailed simulation.

The simulation was done with OSCAR 3_9_8 in which the CustomParticle package was implemented to allow for stable massive particles. Digitization and reconstruction was done with ORCA 8_13_1.

3.2 Trigger path

Many trigger paths could be used to ensure the registration of signal events. A natural choice are single muon and double muon triggers. They profit from the presence of high energy staus and stau-muon resemblance. However, if the stau velocity is significantly lower than the speed of light, a wrong bunch crossing could be selected. This feature develops if the stau arrives at the muon detectors with a delay (with respect to a muon of the same momentum) approaching half of the bunch crossings separation. To trigger in a way less dependent on stau properties it is possible to use a jets and $\not{E}_t$ trigger path. It turns out, however, that only $(3.4 \pm 0.3)\%$ of signal events do not pass the single muon HLT trigger selection. It was carefully verified that single muon HLT trigger is built on the first level muon trigger response in the right bunch crossing (L1 single muon trigger accept). Only for $(0.8 \pm 0.2)\%$ of events the single muon trigger gives a response for a wrong (next) bunch crossing and does not for the right one. These events do not pass single muon HLT selection.

In the end, the single muon HLT selection was chosen for the stau analysis chain.

3.3 Selection

As is the case with neutralino NLSP, most of the supersymmetric events originate from squark and gluino production. Each cascade decay of a heavy supersymmetric particle ends on a stau. For large a $c\tau$ the $\tilde{\tau}_1$ have a minimal probability of decay inside the CMS detector.

The selection in the long-lived $\tilde{\tau}_1$ analysis chain is twofold. The first part depends only on the stau/muon candidate properties. At the preselection level, candidate momentum is required to be above $80\,\text{GeV}$ and a barrel muon geometric acceptance cut $|\eta| < 1.2$ is applied. These criteria are motivated by the fact, that only drift tubes present in the barrel muon stations can be used for a time of flight measurement and that low β staus are not reconstructed by the standard moun reconstruction. At the final selection level only tracks that pass quality selection cuts that are described in the next subsection (Sec. 3.4) are accepted. The second part of the selection depends on the whole event. On top of the HLT preselection we require two high transverse momentum muons with an invariant mass well above the Z^0 boson mass, and a large effective event mass M_{eff}, defined as the scalar sum of missing transverse momentum and transverse momenta of three most energetic jets. The selection procedure can be summarized as follows:

1. Preselection

   (a) Event: HLT single muon trigger;
   (b) Track: momentum above 80 GeV;
   (c) Track: $|\eta| < 1.2$;

2. Selection

   (a) Track: quality requiremnts (Sec. 3.4);
   (b) Event:
       i. Effective event mass: $M_{\text{eff}} > 360\,\text{GeV}$;
       ii. Mass of the pair of muon candidates: $M_{\mu\mu} > 110\,\text{GeV}$;
       iii. Transverse momentum of the second hardest muon candidate: $p_T^{2\mu} > 60\,\text{GeV}$;

The influence of the selection on the distributions of the quantities listed above is shown in Figures 13 and 14.
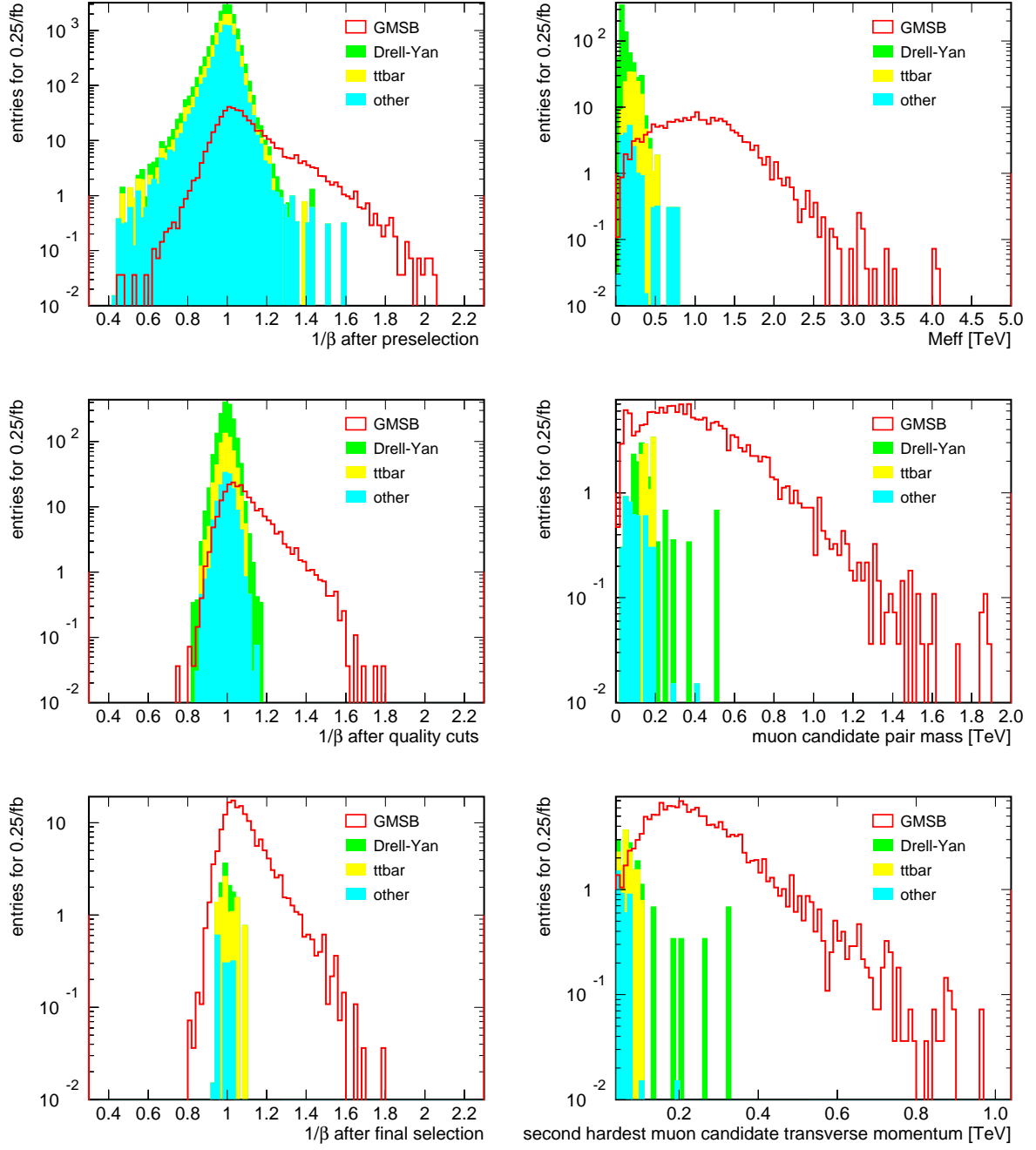
Figure 13: $\tilde{\tau}_1$ NLSP point: $\Lambda = 50\,\mathrm{TeV}$ $m_{\tilde{\tau}_1} = 152.31\,GeV$. Left column: β^{-1} distributions at different stages of the selection. Right column: distributions of selection variables after all cuts but the cut on the plotted variable.
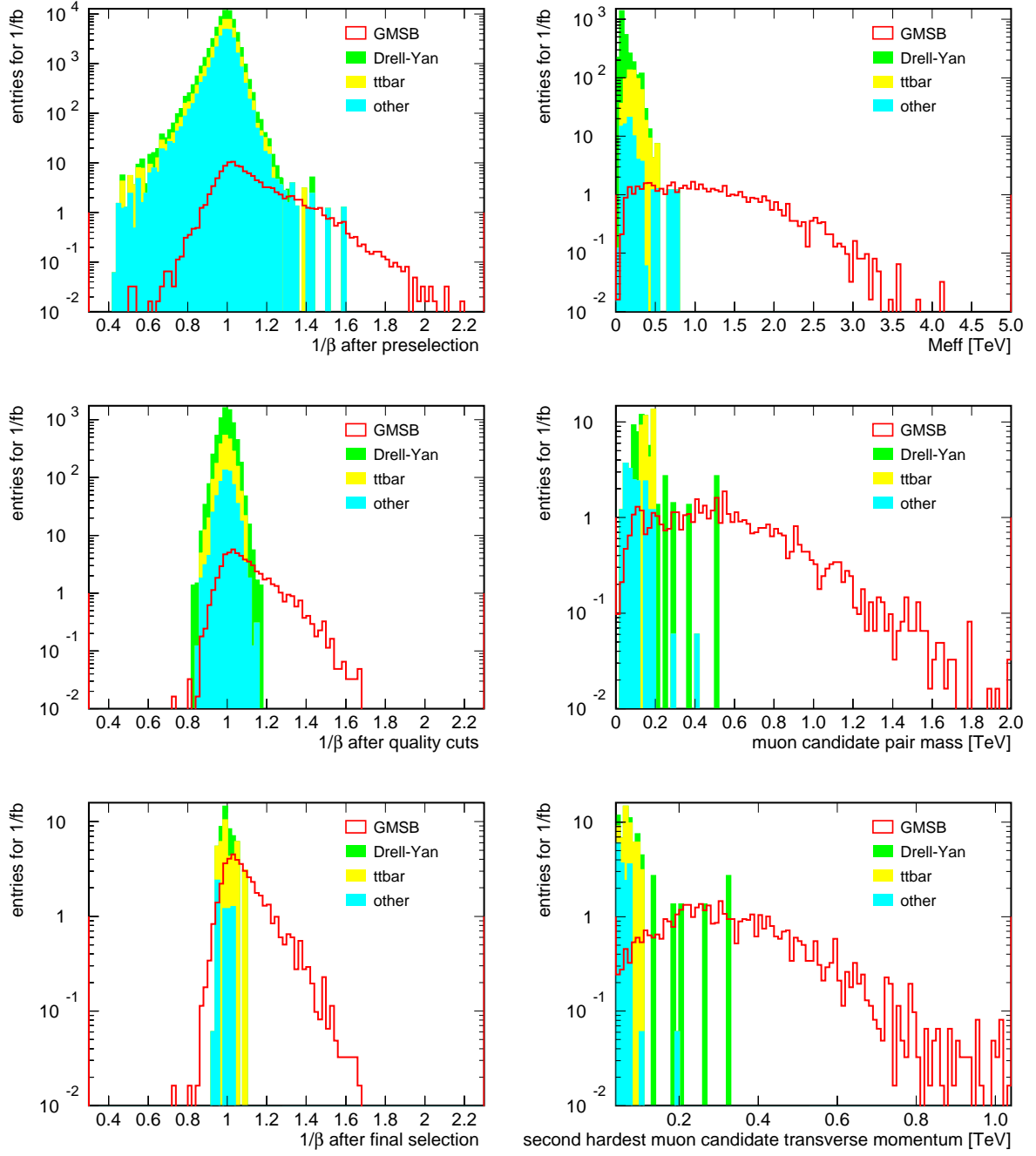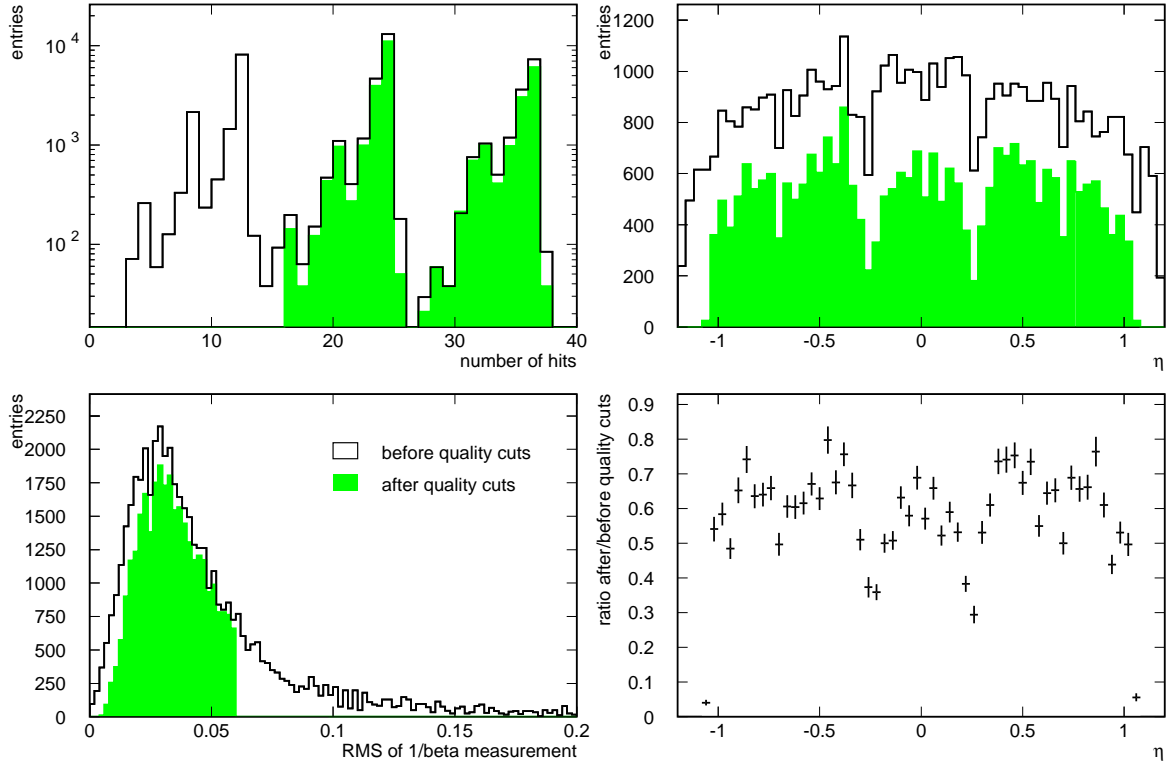
Figure 14: $\tilde{\tau}_1$ NLSP point: $\Lambda = 80\,\mathrm{TeV}\ m_{\tilde{\tau}_1} = 242.93\,GeV$. Left column: β^{-1} distributions at different stages of the selection. Right column: distributions of selection variables after all cuts but the cut on the plotted variable.

Figure 15: Illustration of the effect of the quality selection on muon and stau candidates from the signal sample. Distribution before and after applying quality requirements: overall number of hits (top left), signed difference RMS (bottom left), η (top right) and ratio of η distributions (bottom right).

3.4 The time delay - charged WIMP signature

Long-lived staus behave as "heavy muons". They differ from muons by having lower velocity β. The CMS detector can directly determine their velocity by a time of flight measurement using the Drift Tubes (DT) of the Muon Barrel Stations. The barrel muon system is described in detail elsewhere [8]. Here, we present only the simplest method of measuring the time of flight without altering the DT reconstruction algorithms.

What the drift tube actually measures is not a position of the charged track crossing it but the drift time of the ionization electrons to the sensitive wire. In order to precisely determine the coordinate along the drift direction, the time of the arrival of the particle at the tube must be known.

The knowledge of a coarse $\mathcal{O}(10\,\mathrm{cm})$ coordinate along the sensitive wire is sufficient for muons, because the position of the tube, the velocity of the muon ($\beta \sim 1$), the drift velocity and the velocity of signal propagation along the wire are all known. If the particle velocity is significantly lower than the speed of light, then the points reconstructed in successive DT layers with the assumption $\beta = 1$ will not align because they have a time delay δ_t. They will be reconstructed as displaced by δ_x in the direction opposite to the drift direction. The relation between δ_x and δ_t is the following

$$\frac{\delta_x}{v_{\mathrm{drift}}} = \delta_t = t_{\beta<1} - t_c = \frac{L}{c}\left(\frac{1}{\beta} - 1\right) \tag{26}$$

and hence

$$\frac{1}{\beta} = 1 + \frac{\delta_x}{L}\frac{c}{v_{\mathrm{drift}}} \tag{27}$$

where L is the flight distance and v_{drift} is the drift velocity.

The highest order primitive that can be returned by a DT station is the 4D segment, which combines the information from two perpendicular superlayers: r-ϕ consisting of 8 DT layers (two r-ϕ superlayers in one station are taken as one double superlayer) and r-z consisting of 4 DT layers. After matching, the position in both perpendicular directions is known sufficiently well to precisely calculate the expected muon arrival time.

Candidate track β^{-1} is estimated in the following way.

In the first step, for each superlayer j which has at least 3 associated rec-hits, a corrected local track segment (2d rec-hit) is analytically calculated, taking into account the possibility that the particle causing it was off-time.

For this purpose, regression lines for left and right hits are separately determined

$$x_{ij}^L = a_j^L + b_j^L \cdot z_{ij}, \quad x_{ij}^R = a_j^R + b_j^R \cdot z_{ij}, \tag{28}$$

where x_{ij}^L, (x_{ij}^R) is left (right) rec-hit local coordinate along drift direction, z_{ij} is local layer position and $a_j^{L/R}, b_j^{L/R}$ are regression parameters. Rec-hit is called "left" or "right" depending on which ambiguous position is associated to the track. For left (right) rec-hits the difference $x_{ij} - x_{ij}^{\text{wire}}$ is negative (positive).

If there is only one left or one right hit then a pseudo-regression line is drawn parallel to that calculated for opposite hits ($b_j^L = b_j^R$). Determination of β^{-1} is not possible if there are only left or only right hits in the superlayer.

Finally, the corrected 2d rec-hit is determined taking average values

$$a_j = \frac{a_j^L + a_j^R}{2}, \quad b_j = \frac{b_j^L + b_j^R}{2}. \tag{29}$$

and used to obtain β^{-1} estimate for each rec-hit i in the superlayer j:

$$\left(\frac{1}{\beta}\right)_{ij} = 1 + \frac{c}{v_{\text{drift}}} \frac{(\delta_x)_{ij}}{L_{ij}}, \tag{30}$$

where $(\delta_x)_{ij} = |x_{ij} - x_{ij}^{\text{wire}}| - |a_j + b_j \cdot z_{ij} - x_{ij}^{\text{wire}}|$ and L_{ij} is the flight distance between the interaction point and the rec-hit. Drift velocity is taken to be equal to that used for simulation $v_{\text{drift}} = 53.4\,\mu\text{m/ns}$.

For each superlayer j with n_j rec-hits, there are $n_j - 2$ independent β^{-1} measurements, because two parameters a_j, b_j are determined at the same time. Taking this into account, final β^{-1} estimate is obtained by a proper weighted average, which takes the whole available information form N_{SL} superlayers into account:

$$\left\langle \frac{1}{\beta} \right\rangle = \frac{\sum_{j=1}^{N_{SL}} \frac{n_j-2}{n_j} \cdot \sum_{i=1}^{n_j} \left(\frac{1}{\beta}\right)_{ij}}{\sum_{j=1}^{N_{SL}} (n_j - 2)} \tag{31}$$

The dispersion of this measurement

$$\sigma\left(\frac{1}{\beta}\right) = \frac{\sqrt{\sum_{j=1}^{N_{SL}} \frac{n_j-2}{n_j} \cdot \sum_{i=1}^{n_j} \left\{\left(\frac{1}{\beta}\right)_{ij} - \left\langle\frac{1}{\beta}\right\rangle\right\}^2}}{\sum_{j=1}^{N_{SL}} (n_j - 2)} \tag{32}$$

is taken as an estimate of its precision. Using background muons it was checked that a Gaussian fit to the pull distribution $(\langle\beta^{-1}\rangle/-1)\sigma(\beta^{-1})$ has a central value of -0.117 ± 0.006, sigma 1.145 ± 0.005 and $\chi^2/\text{ndf} = 1.03$. The goodness of the fit ensures, that the method described above correctly measures particle velocities. The sigma of the pull distribution is 15% too high, which means that errors are under determined. These errors are corrected for the purpose of stau mass determination described in the next subsection. The central value of the pull distribution is shifted down by $0.1 \cdot \sigma$. The most probable reason for this effect is presence of δ electrons and other additional activity inside muon stations. The measurement is deteriorated by association of a background rec-hit to the track mainly if δ electron and muon are so close, that only one hit is reconstructed and δ electron is closer to the wire than muon. If this happens, a muon looks as if it was travelling a bit faster than light.

In order to avoid backgrounds due to wrongly measured muons, the following quality requirements are applied.

1. Hits in the fourth muon station, equipped only with $r - \phi$ superlayers, are not used.

2. Only superlayers giving at least one hit on the left side of the wires and at least one on the right side are taken into account. This requirement eliminates the situation in which only left or only right hits are selected in a given superlayer for a very low β particle.

3. The overall number of hits must be greater than 15.

24

Table 5: Numbers of candidates expected for integrated luminosity $\mathcal{L} = 1/\text{fb}$ at different stages of the selection: preselection → point 1 on the page 20; track quality → quality requirements described in the Section 3.4; event selection → point 2b on the page 20; β^{-1} signal region → $\beta^{-1} > 1.132$.

dataset	preselection	track quality	event selection	β^{-1} signal region
su05_L50_M100_stau	1714.1	956.4	666.4	155.054
su05_L80_M160_stau	108.8	59.8	45.0	12.019
hg03_DY2mu_shat115	8105.6	4422.6	13.6	0.012
mu03_tt2mu	2686,0	1624.4	33.7	0.029
mu03_WW2mu	573.7	327.7	6.0	0.005
mu03_ZZ2mu	202.0	110.1	0.1	0.000
mu03_ZW2mu	231.6	121.3	0.0	0.000
Σ	11798.9	6606.1	53.4	0.046

4. The error $\sigma(\beta^{-1})$ must be smaller than 0.06.

The effect of applying the quality cuts described above is shown in Figure 15 and could be spotted in Figures 13 and 14 where β^{-1} background distributions shows drastic elimination of tails after the quality selection (compare top-left and middle-left panels of Fig. 13, 14).

3.5 Signal significance

In the upper part of Figures 16 and 17 scatter plots β^{-1} versus momentum for GMSB $\tilde{\tau}_1$ NLSP points: $\Lambda = 50\,\text{TeV}$ and $\Lambda = 80\,\text{TeV}$ are shown.

There are no candidates above $\beta^{-1} > 1.8$ not because of the plot limits, but due to pattern recognition that is not aware of the possible presence of low β particles or, more generally, off-time particles. Rec-hits detected for such slow particles do not pass a χ^2 cut used in the official code for local segment (2d rec-hit) reconstruction. Usually only left or only right hits are associated to the local segment. The longer the flight distance to the muon station, the lower β^{-1} particle could have a 2d rec-hit passing our quality cuts reconstructed. Long ago it was pointed out [9] that the use of signed χ^2 with simultaneous delay determination could not only eliminate this efficiency deterioration but also could help in DT system alignment and drift velocity monitoring.

Each of the scatter plots in Figures 16 and 17 is a result of one pseudo-experiment, in which candidates form signal and background datasets were randomly selected with a probability corresponding to the integrated luminosity $\mathcal{L} = 0.5/\text{fb}$ and $\mathcal{L} = 4/\text{fb}$ respectively.

Horizontal lines are drawn for the muon expectation: $\beta_\mu^{-1} = 1$ and $\beta_\mu^{-1} \pm 3\sigma = 1 \pm 0.132$, whereas, the falling lines are drawn for the stau expectation $\beta_{\tilde{\tau}_1}^{-1}$ and $\beta_{\tilde{\tau}_1}^{-1} \pm 2.5\sigma$. The region farther away from muon expectation than 3σ and closer to stau expectation than 2.5σ is highlighted.

Numbers of expected events for an integrated luminosity of $\mathcal{L} = 1/\text{fb}$ at different stages of the selection procedure are given in Table 5. There is no background events left in the $\beta^{-1} > 1.132$ signal region.

The numbers given in the last column in the table are an estimate obtained by multiplying the number of events at the "event selection" stage by an efficiency corresponding to applying the β^{-1} selection directly after the "track quality" selection. The expected number of background events is so small, that a study of its systematics cannot influence significance determination. This is however true only if the simulation of DT takes into account all problems that could show up during data taking. It is obvious that prior to performing the described analysis, the behavior of DT system must be studied in detail with real data. Fortunately all muons could be used for such studies and there are pure sources of energetic muons like $Z \to \mu^+ \mu^-$ decays. The idea is to tune quality cuts in a way to completely suppress tails above $\beta^{-1} > 1.132$ for Z muons. Again it is not possible to know an efficiency of such requirement before LHC startup.

Finally, the upper limit for the number of expected background events in the signal region is evaluated to be 0.05 events for 1/fb. Using the $S_{c12} = 2(\sqrt{s+b} - \sqrt{b})$ significance estimator [10] a 5σ discovery could be obtained with 8 signal events. This corresponds to $\mathcal{L} = 52/\text{pb}$ for GMSB point $\Lambda = 50\,\text{TeV}$ and $\mathcal{L} = 667/\text{pb}$ for $\Lambda = 80\,\text{TeV}$. It means that with an integrated luminosity of $\mathcal{L} = 10/\text{fb}$ it will be possible to discover GMSB SUSY from SPS 7 line for at least $\Lambda = 120\,\text{TeV}$.
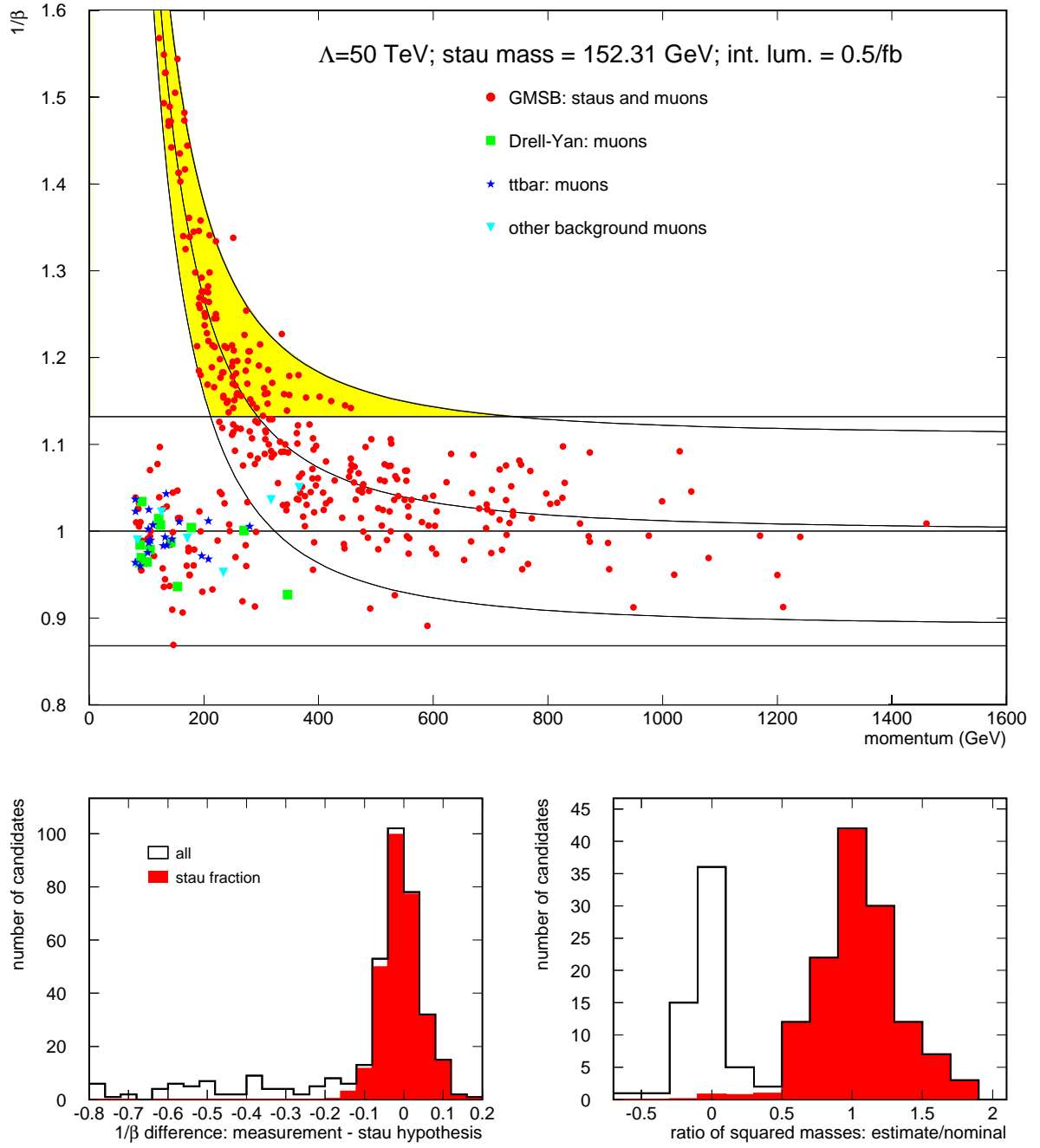
Figure 16: Results of one pseudoexperiment for $\tilde{\tau}_1$ NLSP point $\Lambda = 50\,\mathrm{TeV}$, $m_{\tilde{\tau}_1} = 152.31\,\mathrm{GeV}$ ($\mathcal{L} = 0.5/\mathrm{fb}$). Top: β^{-1} versus momentum. Full circles: staus and muons from signal; squares: Drell-Yan bckg.; stars: $t\bar{t}$ bckg.; triangles: intermediate boson pairs bckg. (The meaning of the superimposed lines and the highlighted area is described in the text.)
Bottom left: difference between β^{-1} measured and β^{-1} expected for $\tilde{\tau}_1$.
Bottom right: mass squared normalized do nominal mass squared plotted for candidates in a momentum interval (122 GeV, 332 GeV).
Dark regions on bottom plots correspond to $\tilde{\tau}_1$ fraction attributed by the fit described in the Section 3.7.
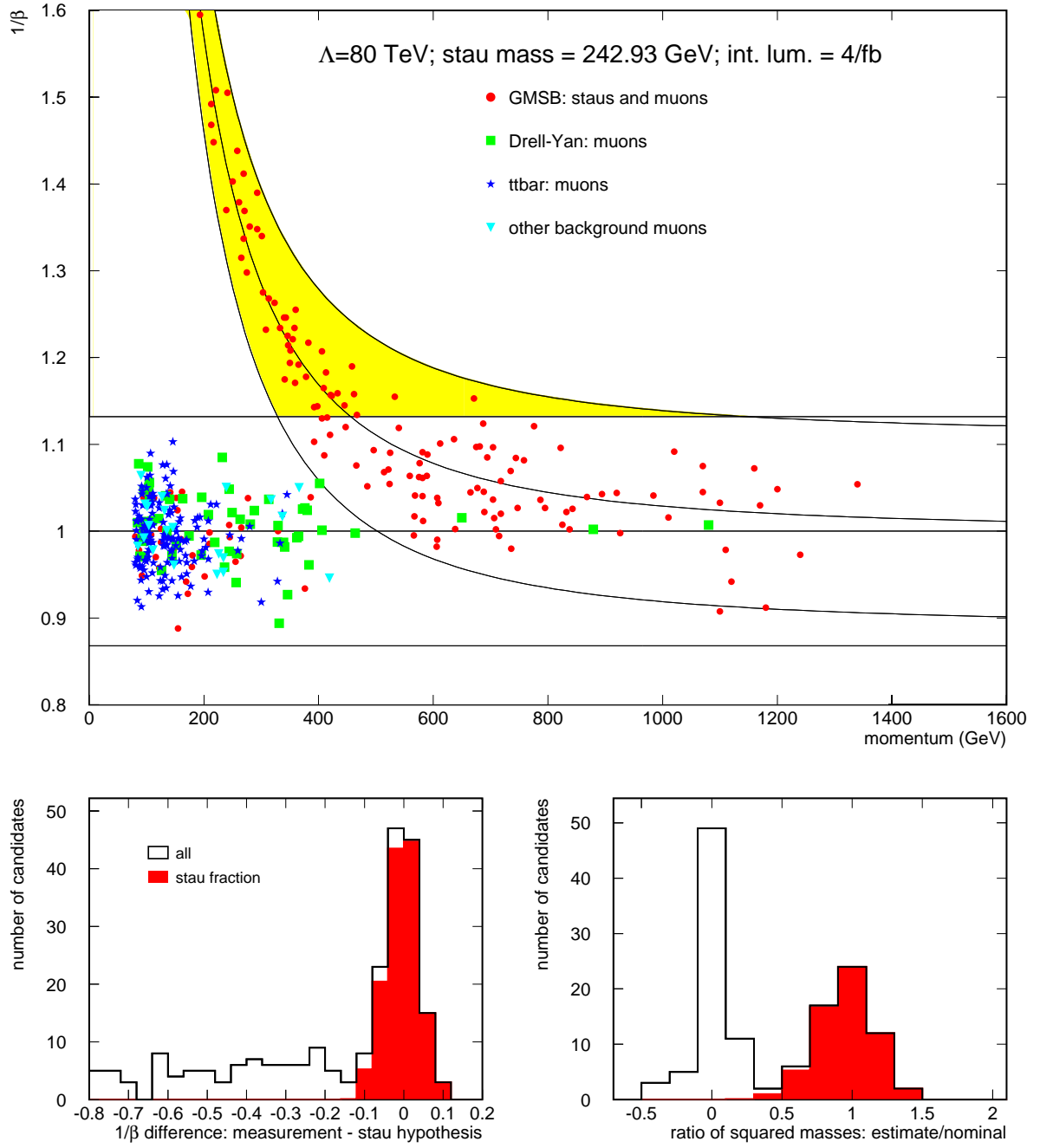
Figure 17: Results of one pseudoexperiment for the $\tilde{\tau}_1$ NLSP point $\Lambda = 80\,\mathrm{TeV}, m_{\tilde{\tau}_1} = 243.93\,\mathrm{GeV}$ ($\mathcal{L} = 4$/fb).
Top: β^{-1} versus momentum. Full circles: staus and muons from signal; squares: Drell-Yan bckg.; stars: $t\bar{t}$ bckg.; triangles: intermediate boson pairs bckg. (The meaning of the superimposed lines and the highlighted area is described in the text.)
Bottom left: difference between β^{-1} measured and β^{-1} expected for $\tilde{\tau}_1$.
Bottom right: mass squared normalized to the nominal mass squared plotted for candidates in a momentum interval (195 GeV, 530 GeV).
Dark regions on bottom plots correspond to $\tilde{\tau}_1$ fraction attributed by the fit described in the Section 3.7.

27

Figure 18: $1/\beta - 1$ measurement for pseudo-cosmic muons as a function of their time delay at the CMS origin. Light gray: outward going muons. Dark gray: inward going muons.
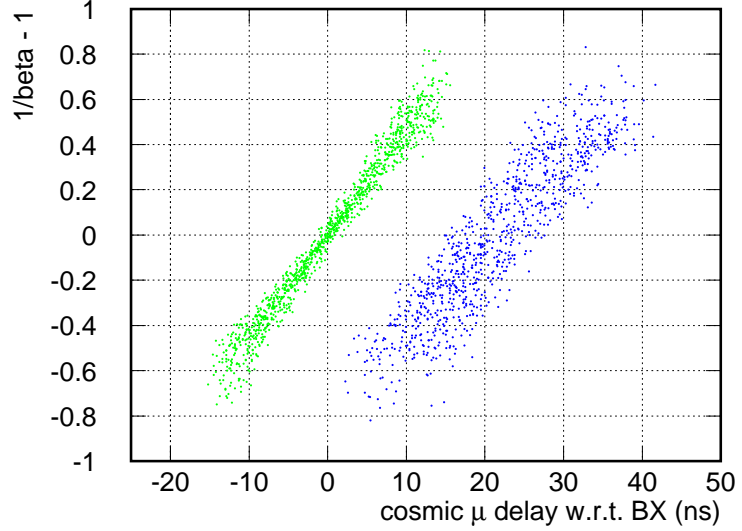
3.6 Cosmic muon background

Cosmic muons are a natural source of background in a search for delayed particles. Having this in mind, the present analysis was designed to completely eliminate this background. The simple requirement of a presence of two muons with $p_T > 60$GeV and invariant mass above $110\,$GeV is equivalent to the necessity of simultaneous observation of a cosmic muon and a hard muon from the underlying event. The expected rate of LHC muons above $p_T > 60$GeV is lower than 2Hz at a luminosity of $\mathcal{L} = 10^{33}cm^{-2}s^{-1}$ [11]. However, a cosmic muon could be seen by the DT system if its delay w.r.t. the bunch crossing is between $-15\,$ns and $+40\,$ns. Hence, the coincidence rate should be doubled. This means, that the rate of cosmic muons accepted by the present analysis will be lower than the cosmic muon rate (CM rate) by a factor of at least $f_\mu = 40\,$MHz$/4\,$Hz $= 1 \cdot 10^7$.

It was shown [12] that the rate of cosmic muons above $10\,$GeV entering CMS is $47\,$kHz on the surface (MTCC configuration) and that the underground rate is lower due to the average loss of $50\,$GeV
and is expected to be around $3\,$kHz. In our analysis we accept muons above $p > 80\,$GeV. The rate of such muons underground should correspond to the rate of muons above $p > 130\,$GeV on the surface. Taking into account known shape of momentum dependence of the cosmic muon rate [13] one could estimate that the ratio of the muon rates is equal to $R_{p>10\,\mathrm{GeV}}/R_{p>130\,\mathrm{GeV}} = \{12/(10\,\mathrm{GeV})^2\}/\{25/(130\,\mathrm{GeV})^2\} = 81$. This gives an upper limit on the rate of cosmic muons with momentum above $p > 130\,$GeV entering CMS underground $R_{p>80\,\mathrm{GeV}}^{\mathrm{undergr.}} = 47\,kHz/81 = 580\,Hz< 1\,$kHz.

Using the factor estimated above f_μ one can expect, after one LHC year of data taking (10^7 s), $1\,$kHz$\cdot 10^7\,$s$/1 \cdot 10^7 = 1000$ background events. This number could be drastically reduced if very loose requirement of candidate track agreement with a 5σ beam spot $100\mu m \times 38cm$ is introduced. Since CM rate is proportional to the horizontal cross section it will give a reduction factor of $f_{\mathrm{bs}} = 280\mathrm{m}^2/0.38\mathrm{cm}^2 \approx 7 \cdot 10^6$. If a requirement of at least two pixel hits is applied then the reduction is $f_{\mathrm{pix}} = 280\,\mathrm{m}^2/700\,\mathrm{cm}^2 = 4 \cdot 10^3$.

Finally, we can estimate that after one year of operation one could expect less than $1\,$kHz $\cdot\, 10^7$s$/f_\mu/f_{\mathrm{pix}} = 1/4$ events due to a cosmic muon accepted if only the requirement of pixel hits would be applied and less than $1/7000$ if loose beam constraint would be used.

We can conclude, that cosmic muons do not contribute to the background for the present study. Nevertheless, it is interesting to see how energetic cosmic muon could be seen by CMS. To visualize this we used Drell-Yan fully simulated muons and changed their timing randomly by $\pm 50\,rmns$. We have done that two times. Once without changing the direction of muons, which simulates outward going pseudo-cosmic muons and once changing the direction to the opposite one, which simulates inward going pseudo-cosmic muons. This change of direction is done by adding a time shift $\Delta t = -L_{\mathrm{hit}}/c$ prior to the random time shift, where L_{hit} is the distance from the hit position to the CMS origin.

We have applied the quality requirements to the pseudo-cosmic muons (including the standard χ^2 cut) and calculated in the same way, as in the analysis their "velocity". In Figure 18 we plot the measured $1/\beta - 1$ (which

should be equal to zero for LHC muons) with respect to the time delay at the CMS origin. There are two branches of points in the scatter plot. The first (light gray points), going through point (0,0), is for outward going pseudo-cosmic muons. The second (dark gray points), is for inward going muons. The spread of the second branch is greater because these muons are going in the "wrong" direction and so the time shift (the difference between the actual arrival time and the time expected for the particle created at the origin at the time of bunch crossing) is changing between muon stations. This spread could be eliminated using an algorithm which takes into account the possibility, that the registered track is due to inward going muon.

There are (almost) no points for $|1/\beta - 1| > 0.8$ because of the χ^2 cut. All points in the scatter plot are pseudo-cosmic muons, that should be seen by the standard standalone reconstruction. However, because of the finite tracker time resolution, only the part with a delay around zero will also have tracker information. It is interesting to see, that for a delay of 10 ns the same cosmic muon could be seen as a "normal" pair of muons in the central tracker, as a "tachyonic" muon in the upper half of CMS and as a "massive" muon in the lower part. Finally, cosmic reconstruction/reduction could be done offline, by reconstructing the whole trajectory using DT data not used by standard reconstruction due to too large time delay.

3.7 Stau mass determination

In this section simultaneous sample composition and stau mass determination will be described. High momentum parts of the distributions shown in the upper part of Figures 16 and 17 are dominated by stau candidates. It can be seen from the bottom left panel of these figures, where the difference between measured β^{-1} and β^{-1} expected for stau is plotted. A clear peak around zero is possible only if there is no genuine muons in the region where muon and stau expectations are close one to another.

The measurement of β^{-1} and momentum of a particle can be transformed into a mass squared estimate because $\beta^{-1} = E/p$ and hence

$$ m^2 = p^2 \cdot \left(\frac{1}{\beta^2} - 1 \right). \tag{33} $$

The distributions of the ratio of the mass squared estimate and nominal mass squared is shown in the bottom right panels the figures. To underline clear stau – muon separation only the momentum intervals (122 GeV,332 GeV) and (195 GeV,530 GeV) were used. For lower momenta there are no stau candidates (due to the not signed χ^2 selection used for rec-hit reconstruction, as described in the preceding Section). For higher momenta the tails of the distributions begin to overlap.

The fraction of staus grows with the candidate momentum. The background composition and signal distribution will not be well known at the LHC startup. We try to be as close as possible to the real situation and perform a blind composition fit without any prior knowledge. To account for a changing stau to muon ratio we estimate the composition separately in four momentum intervals defined by momenta corresponding to $\beta^{-1} = 1.60, 1.40, 1.25, 1.15, 1.10$ for the stau hypothesis. These momenta are 122, 155, 203, 268, 332 GeV for $\Lambda = 50$ TeV and 195, 248, 324, 428, 530 GeV for $\Lambda = 80$ TeV. Candidates with higher momenta, for which stau–muon separation is small $\beta^{-1}(\tilde{\tau}_1) - \beta^{-1}(\mu) < 0.1$, are not used for stau mass determination. It was checked that the exact choice of momentum intervals has no statistically significant influence on the results.

To estimate the stau mass from data a likelihood fit of signal composition was performed. The following description of the composition was used

$$ \mathcal{F}(\beta^{-1}(i), \sigma(i), p(i); m, f_1, f_2, f_3, f_4) = \begin{array}{ll} (1 - f_{j(i)}) & \cdot \quad \mathcal{G}(\beta^{-1}(i); 1, \sigma(i);) \\ + \quad f_{j(i)} & \cdot \quad \mathcal{G}(\beta^{-1}(i); \beta^{-1}(m, p(i)), \sigma(i)) \end{array} \tag{34} $$

where $\beta^{-1}(i)$, its error $\sigma(i)$ and momentum $p(i)$ are measured values for each candidate i; stau mass m, which enters via the relation $\beta^{-1}(m, p(i)) = \sqrt{\frac{m^2}{p(i)^2} + 1}$ and stau fractions $f_{j=1,4}$ are free parameters. $\mathcal{G}(x; \langle x \rangle, \sigma_x)$ is a Gaussian resolution function.

The minimized function was

$$ \mathcal{L} = -2 \sum_i \log \left\{ \mathcal{F}\left(\beta^{-1}(i), p(i); m, \sigma(i), \vec{f} \right) \right\}. \tag{35} $$

The result of 1000 pseudo-experiments performed for an integrated luminosity of $\mathcal{L} = 0.5$/fb ($\mathcal{L} = 4$/fb) for the GMSB point $\Lambda = 50$ TeV ($\Lambda = 80$ TeV) is shown in the left (right) side of Figure 19.

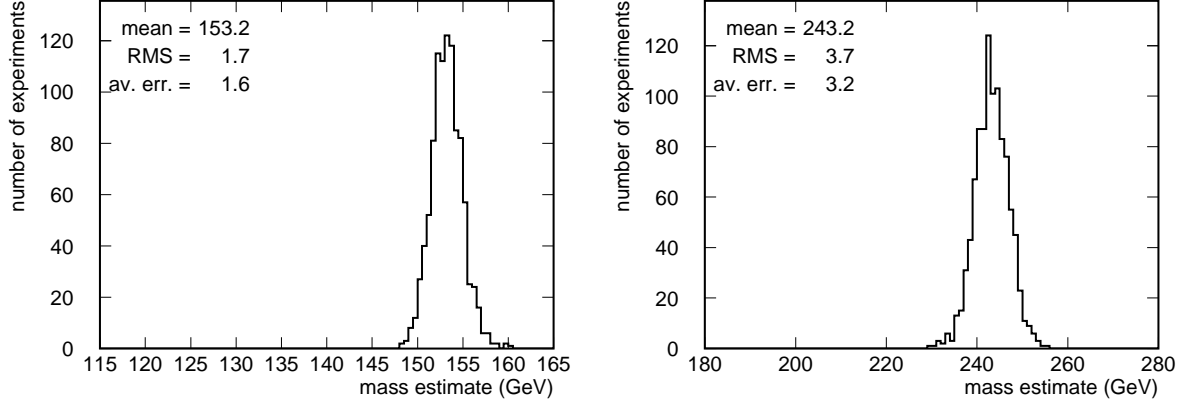Figure 19: Mass estimate distribution from 1000 pseudo-experiments for $\tilde{\tau}_1$ NLSP point $\Lambda = 50\,\mathrm{TeV}$, $m_{\tilde{\tau}_1} = 152.31\,\mathrm{GeV}$ ($\mathcal{L} = 0.5/\mathrm{fb}$) and $\Lambda = 80\,\mathrm{TeV}$, $m_{\tilde{\tau}} = 243.93\,\mathrm{GeV}$ ($\mathcal{L} = 4/\mathrm{fb}$).

The average, returned by the fit error: $1.6\,\mathrm{GeV}$ for $\Lambda = 50\,\mathrm{TeV}$ ($3.2\,\mathrm{GeV}$ for $\Lambda = 80\,\mathrm{TeV}$) is in agreement with the RMS of the distribution of the mass estimate: $1.7\,\mathrm{GeV}$ (respectively: $3.7\,\mathrm{GeV}$). Hence, the error returned by the fit can be trusted to be an estimate of the statistical error.

The following systematic effects could influence the result

- inefficiency for large measured β^{-1};

- bias due to δ electrons;

- possible bias of the momentum measurement for staus.

The agreement between the estimated and nominal stau masses shows that the net systematic effect is smaller than the statistical error. As a measure of the relative systematic error we take the larger relative difference between the estimated and nominal stau masses: (153.2-152.3)/152.3=0.59%. The final result is:

$$
\begin{aligned}
M_{\tilde{\tau}_1}^{\mathrm{est.}} &= \{153.2 \pm 1.6(\mathrm{stat.}) \pm 0.9(\mathrm{syst.})\}\,\mathrm{GeV} \quad \text{at}\, \mathcal{L} = 0.5/\mathrm{fb} \quad \text{for}\, M_{\tilde{\tau}_1}^{\mathrm{gener.}} = 152.31\,\mathrm{GeV} \\
M_{\tilde{\tau}_1}^{\mathrm{est.}} &= \{243.2 \pm 3.2(\mathrm{stat.}) \pm 1.4(\mathrm{syst.})\}\,\mathrm{GeV} \quad \text{at}\, \mathcal{L} = 4/\mathrm{fb} \qquad \text{for}\, M_{\tilde{\tau}_1}^{\mathrm{gener.}} = 242.93\,\mathrm{GeV}
\end{aligned}
\tag{36}
$$

4 Conclusions

Two scenarios giving nonstandard detector signatures of Gauge-Mediated Supersymmetry Breaking models were analyzed.

In the first one, the neutralino $\tilde{\chi}_1^0$ is the next to lightest supersymmetric particle. It decays inside the detector into a photon and a gravitino. We used the non-pointing photon signature in the ECAL to search for a signal. We showed that for a point with the cross section of the order of 500 pb and an integrated luminosity of 10/fb the $\tilde{\chi}_1^0$ lifetime could be determined with a precision of the order of 20% for a $c\tau$ range from centimeters to meters. The minimal integrated luminosity needed for 5σ discovery was estimated to be $\mathcal{L} = 3.5/\mathrm{fb}$ for the simulated model and the minimal cross-section allowing for discovery at $\mathcal{L} = 10/\mathrm{fb}$ as $\sigma = 100\,\mathrm{fb}$.

In the second case the long-lived stau $\tilde{\tau}_1$ is the NLSP. We show that CMS muon system is able to identify it as a particle traveling with a velocity lower than the speed of light using standard information delivered by the Drift Tubes of the Barrel Muon System. We showed, that it is possible to determine stau mass with a precision of few percent.

5 Acknowledgments

References

[1] L. Alvarez-Gaumé, M. Claudson and M.B. Wise,
Low-Energy Supersymmetry Nucl. Phys. **B207**(1982)96-110

[2] R. Culbertson *et al.*, *Low-Scale and Gauge-Mediated Supersymmetry Breaking at the Fermilab Tevatron Run II*, FERMILAB-Pub-00/251-T, hep-ph/0008070

[3] B.C. Allanach *et al.*, *The Snowmass Points and Slopes: Benchmarks for SUSY Searches*, CERN-TH/2002-020, hep-ph/0202233

[4] G. Franzoni, *The electromagnetic calorimetric of CMS and its sensitivity to non-pointing photons*,
PhD Thesis, Univ. Statale Milano - Univ. Milano Bicocca, 2004-2005

[5] M. Spiropulu, T. Yetkin, *Inclusive missing transverse energy + multijet SUSY search at CMS*, CMS-AN-2006/089

[6] M. Spiropulu, T. Yetkin *Evaluation of the Missing Transverse Energy shape systematic uncertainty due to tails in the jet resolution at CMS*, CMS-IN-2006-015

[7] B. Scurlock, D. Acosta, P. Bartalini, R. Cavanaugh, A. Drozdetskiy, A. Korytov, K. Kotov, K. Matchev, G. Mitselmakher, Y. Pakhotin, M. Schmitt, *CMS Discovery Potential for mSUGRA in Single Muon Events with Jets and Large Missing Transverse Energy in pp Collisions at sqrt(s)=14 TeV*, CMS-AN-2006/083

[8] CMS Collaboration, *CMS Physics TDR Volume I: Detector Performance and Software*
CERN/LHCC 2006-001, CMS TDR 8.1

[9] M. Kazana, G. Wrochna and P. Zalewski, *Study of the NLSP from the GMSB Models in the CMS Detector at the LHC*, CMS CR-1999/019 – PHYSICS PH-SUSY

[10] CMS Collaboration, *CMS Physics TDR Volume II: Physics Performance*,
CERN/LHCC 2006-021, CMS TDR 8.2

[11] CMS Collaboration, *The Trigger and Data Acquisition project, Volume II: Data Acquisition & High-Level Trigger*,
CERN/LHCC 2002-26, CMS TDR 6.2

[12] V. Drollinger, *The Cosmic Muon Generator Manual and Validation Plots*, CMS IN 2005/016

[13] P. Achard *et al.*, L3 Collaboration, *Measurement of the atmosferic muon spectrum form 20 to 2000 GeV*,
Phys. Lett.**B598**(2004)15-32